

Development and Test of the Langmuir Electric Field Array

By

Jianhua Zhang

Submitted in Partial Fulfillment
of the Requirements for the Degree of
Master of Science in Electrical Engineering

New Mexico Institute of Mining and Technology
Department of Electrical Engineering
Socorro, New Mexico
January, 2010

ABSTRACT

The Langmuir Electric Field Array (LEFA) is a network of broadband electric-field (E-field) change sensors and is being developed to achieve a deeper understanding of individual lightning flashes and the entire thunderstorm. Each station within the network consists of a field-change meter, GPS unit, data acquisition module (DAM), solar power module and wireless communication module. The stations are designed to be rugged for extended operation in remote, wet environments. GPS provides accurate common time to all stations in the network.

This thesis presents analysis, characterization and calibration of the sensors used to measure changes in E-field. There are three channels each with separate antenna and gains to detect the E-field over a different range of distances. The channels are denoted “sensitive,” “medium,” and “insensitive” which corresponds to the size of antenna and gains on each channel. Analysis of each channel was performed to calculate the gain of each channel, corresponding theoretical maximum value of the E-field that could be measured on each channel and how the resulting voltage related to the E-field value. Three forms of calibration were performed: self-calibration, cross-calibration and distance dependent calibration. Self-calibration was performed to determine the experimental gain ratios between the three channels on one station by recording the same lightning flashes and taking the ratio of signal strengths between three measurement channels. Cross-calibration was performed by placing several stations at the same location and taking the ratio of recorded signals from the same lightning strikes to get gain ratios across stations. Distance dependent calibration was performed by deploying several stations at individual field locations and comparing the signals obtained on lightning flashes that were remote (more than 100~km distant) from all the stations. A least-squares method was applied to estimate the self-gain and cross-gain ratios in the calibration process.

Results of the self-calibration show that the experimental gain ratios vary from those predicted by 13% for the sensitive-to-medium channel ratio and 149% for medium-to-insensitive ratio. The differences were determined to be due to the difference between the effective area and geometrical area of the sensor plate. Cross-calibration results show that the experimental gain ratios range from between 0.96 and 3.05 for the same channels across stations. These vary from those predicted by 83% at most, which was attributed to the different height of each stand and other geometric factors, still unknown. Well-known lightning return-stroke models separate the electric field into terms dependent on electrostatic charge transfer, return-stroke current and current rate-of-change. The electric field falls off as distance cubed ($1/r^3$) for the electrostatic term, distance squared ($1/r^2$) for the current term and $1/r$ for the term proportional to current rate-of-change. As part of the distance dependent calibration, we also determined that the $1/r$ distance dependent model best fit the data from the remote flashes. For the remote flashes the sensitivity ratio of station2/station6 is 1.32 ± 0.02 . Gain ratio of station4/station6 is 0.65 ± 0.06 ; while station5/station6 is 0.72 ± 0.01 . Gain ratio of station7/station6 is 2.15 ± 0.05 ; finally station8/station6 is 1.02 ± 0.04 . These differences can be largely explained by different electric field concentration factors dependent on the local ground curvatures. The gain ratios that were obtained in distance dependent calibration were used to scale multi-station measurements accordingly and correlate stages of a lightning flash across stations. The results obtained from a storm on October 20, 2009 are reasonable based on our current understanding of cloud-to-ground (CG) and intra-cloud (IC) lightning flashes.

Vocabulary

Acronym	Definition
ASCII	American Standard Code for Information Interchange
A/D	Analog-to-Digital
CG	Cloud-to-Ground
DAM	Data Acquisition Module
DC/DC	Direct Current to Direct Current
delta-E meter	field-change meter, also called 'slow antenna'
ΔE	the change of E-field
ΔQ	the charge changes
E-field	electric-field
EMI	Electrical and Magnetic Interference
FC meter	Field-Change meter
GPS	Global Position System
GPB	GPS signal conditioning Board
GPIO	General Purpose In/Out Pin
GUI	Graphic User Interface
I	Insensitive Channel of slow antenna
IC	Intra-Cloud
kS/sec	kilo-Sample/sec
LASA	Los Alamos Sferic Array
LMA	Lightning Mapping Array
LEFA	Langmuir Electric Field Array
M	Medium Channel of slow antenna
M/I	self-gain ratio between M channel and I channel
MPPT	Maximum Power Point Track
MSL	Mean Sea Level

NCG	Negative CG flash
NLDN	U.S. National Lightning Detection Network
NTP	Network Time Protocol
op amp	operational amplifier
PC-104	an embedded computer standard
PCB	Printed Circuit Board
PCG	Positive CG flash
PPS	Pulse-Per-Second
Puma	Single Board Computer from Versallogic Corporation
Puma#/Puma#	cross-gain ratios between two different stations
PV	photovoltaic
RX	serial receive
S	Sensitive Channel of slow antenna
SAD	Slow A/D converter
Salad-bowl	aluminum contain, its shape looks like a salad-bowl
SBC	Single Board Computer
S/M	self-gain ratio between S channel and M channel
Slow antenna	the instrument to detect the E-field change
TX	serial transmit
UTC	Coordinated Universal Time
VHF	Very High Frequency
WAP	Wireless Access Points
WWLLN	World Wide Lightning Location Network

ACKNOWLEDGMENT

I am heartily thankful to my advisor, Dr. Richard G. Sonnenfeld, for his encouragement, guidance and support throughout my graduate study at New Mexico Tech, which helped me develop a deeper understanding of my thesis project, and his great help on my thesis writing.

Also I offer my regards and blessings to Steve Hunyady, Victor Alvidrez, Keith Morris, Tao Wang, Jeff LaPierre, and Genevieve Vaive, who all supported me in many respects during the course of the project.

I would like to acknowledge other members in my committee group, Dr. Scott Teare and Dr. Kevin Wedeward. They made many suggestions about the engineering part of my thesis.

Finally, I appreciate the great help from my parent, Bulong Zhang and Ying Jiang. I would also like to show gratitude to my husband, Dr. Gaopeng Lu, for many suggestions on data analysis.

Without their help, I could not have finished my graduate study as planned.

TABLE OF CONTENTS

ACKNOWLEDGMENT	ii
CHAPTER 1 Introduction	1
1.1 Overview of Langmuir Electric Field Array (LEFA).....	1
1.1.1 Research Object of LEFA.....	1
1.1.2 Background and Science Goals of LEFA.....	2
1.2 Organization of the Thesis	4
CHAPTER 2 LEFA Requirements and Summary	5
2.1 Requirements of LEFA	5
2.2 Overview of a LEFA Station	9
2.3 Field-Change Meter	11
2.3.1 Mechanical Design of Slow Antenna Sensor	12
2.3.2 Analysis of Circuit of Slow Antenna.....	13
2.4 GPS unit.....	23
2.5 Data Acquisition Module	24
2.5.1 Hardware	24
2.5.2 Sampling Resolution and Sampling Frequency	26
2.5.3 Noise Reduction	28
2.5.4 Data Acquisition Programs.....	29
2.6 Network and Wireless Module.....	30

2.6.1 Network Operations	30
2.6.2 Power Control over the Network.....	32
2.7 Test	32
2.8 Solar Power Module.....	32
2.8.1 Power Budget	33
2.8.2 Performance of Solar Power System.....	34
2.9 Current Configuration of the LEFA Network.....	37
CHAPTER 3 Initial Relative Gain Ratio Calibration	40
3.1 Calibration Site and Theoretical Expectations	40
3.2 Calibration Procedure and Results	43
3.3 Discussion of Results	47
CHAPTER 4 Field Calibration and October 20, 2009 Storm	51
4.1 Noise Reduction	51
4.2 Classical Image Problem.....	52
4.3 Cross-Calibration in the Field	53
4.4 Initial Data Analysis	63
4.4.1 Example of a Multi-Stroke Negative Cloud-to-Ground Flash	63
4.4.2 Example of an Intracloud Flash.....	69
CHAPTER 5 Summary	72
APPENDIX A Schematic of Analog Board -Version B.....	76
APPENDIX B Schematic of Analog Board -Version A	77
APPENDIX C Data-Acquisition-Module (DAM) Datasheet	78

I	DAM Box Basic Components	78
II	DAM Box Layout.....	80
III	DAM Box Connection	81
	APPENDIX D Test Instruction and Form	95
	REFERENCE.....	99

LIST OF FIGURES

Figure 2.1 Picture of Station Puma6 Deployed in k2-EMRTC.....	10
Figure 2.2 Slow Antenna Station Block Diagram.....	11
Figure 2.3 Photo of Sensing Plates Installed on Salad-bowl Slow Antenna	13
Figure 2.4 Schematic of the I-Channel in Salad-bowl Slow Antenna	14
Figure 2.5 Simplified Schematic Diagram of the Circuit of a Slow Antenna.....	16
Figure 2.6 Frequency Responses of Three Channels for Version B Design	19
Figure 2.7 Relaxation and Dedrooping Processes	20
Figure 2.8 Picture of Interior of DAM Box	25
Figure 2.9 Picture of Part Deployment on Base Plate	25
Figure 2.10 Picture of Front Panel	26
Figure 2.11 Sketch of the GPS Signal Conditioning Procedure	27
Figure 2.12 Schematic of the GPS Signal Conditioning Board (GPB)	27
Figure 2.13 Schematic of the filter board	28
Figure 2.14 Schematic of Solar Power Module	33
Figure 2.15 Schematic of Data Logger	36
Figure 2.16 Performance of Solar Power Module	37
Figure 2.17 Current LEFA Network	39
Figure 3.1 Calibration Site at Pound Ranch	41
Figure 3.2 Original Flash from I channel and M channel of 20090727-2350	43

Figure 3.3 Noises from I channel and M channel of 20090727-2350	44
Figure 3.4 Flashes of Both Channels after Low Pass Filter	45
Figure 3.5 Flashes of Both Channels without Boundary Effect	45
Figure 3.6 Result of Least Square Method	46
Figure 3.7 Edge Effect Calculation of I-Channel	48
Figure 3.8 Impact of Height of Stand	49
Figure 3.9 Impact of Arm of Stand	50
Figure 4.1 Classical Image Problem	53
Figure 4.2 Distant Flashes of Puma6 and Puma8	58
Figure 4.3 Distant Flashes by Zooming In	58
Figure 4.4 Fitting Result	58
Figure 4.5 E-field Distortion around Elevated Objects	61
Figure 4.6 The Surface E-field as a Function of Surface Distance	62
Figure 4.7 Drawing of Two Main Processes in NCG	64
Figure 4.8 Original Plots of Six Stations	65
Figure 4.9 Original Plots vs. Dedrooped of Puma2 and Puma5 (Voltage signal)	67
Figure 4.10 Uncalibrated E-field of Puma2 and Puma5 after Dedrooping	67
Figure 4.11 Flashes and Station Locations	68
Figure 4.12 Concept of Reversal Distance	69
Figure 4.13 Drawing of IC flash	70
Figure 4.14 Uncalibrated E-field of six stations after Dedrooping	70
Figure 4.15 Original Plots vs. Dedrooped of Puma4 and Puma5 (voltage signal)	71

LIST OF TABLES

Table 2.1 Parameters of the Operational Amplifiers, AD549JH and LF411	15
Table 2.2 Time Constants of Three Charge Amplifiers of Version B Design	19
Table 2.3 Theoretical Maximum of E-field Measured in Each of Three Channels	22
Table 2.4 Garmin GPS35-LVS Specification	24
Table 2.5 Software that Operates the Data Acquisition and the Network	29
Table 2.6 Data Management Software	30
Table 2.7 Power Budget of Station	34
Table 2.8 Electrical Characteristics of BP 585 Module	36
Table 2.9 Station Names and Locations in Current LEFA Network	38
Table 3.1 Definition of Variables that are referred to in the Calibration.....	40
Table 3.2 Parameters of Version A of Analog Board.....	41
Table 3.3 Configuration of Calibration Stations.....	42
Table 3.4 Self-Calibration Result.....	46
Table 3.5 Cross-Calibration Result of Three Channels.....	47
Table 4.1 Coordinates of Stations in the LEFA Network of October, 2009.....	54
Table 4.2 Locations of Lightning Flashes used in Calibration.....	55
Table 4.3 Theoretical Estimation of Normalized E-field at Each Station.....	56
Table 4.4 Real Calibration Result for Flash A, B, C, E.....	59
Table 4.5 Relative Deviation of Relative Gain Ratio for Flashes A, B, and C.....	60

Table 4.6 NLDN recordings for the negative CG lightning flash.....66

Table 4.7 Distance Range between this NCG flash and stations.....66

CHAPTER 1 Introduction

1.1 Overview of Langmuir Electric Field Array (LEFA)

1.1.1 Research Object of LEFA

Thunderstorms are large, complex geo-systems that operate over a wide range of time and distance scales. The life-cycle of a single cell in a mountain thunderstorm lasts about an hour while a lightning flash occurs over a second or less. Winds, updrafts, and downdrafts in a storm move charge at tens of kilometers per hour, while the wave-front of a lightning return stroke propagates at 200,000 kilometers per second. A thunderstorm contains two sets of processes related to lightning. The first set concerns electrification (also called “cloud charging”), which can last tens of minutes, depending on the intensity of the storm. The second set of processes is discharge processes, which include lightning.

Lightning is a transient, high-current electric discharge whose path length is measured in kilometers. The most common source of terrestrial lightning is the electric charge separated in ordinary thunderstorm clouds [*Uman, 1987*]. In terms of the location where lightning happens, lightning is categorized into two main types, intra-cloud lightning (IC flash) and cloud-to-ground lightning (CG flash).

IC lightning connects positive and negative areas within a single cloud. Intra-cloud lightning is the most common type of lightning. Intra cloud flashes that leave cloud base and approach ground, but do not reach ground, are called air discharges. Such a flash passes through clear air and provides a stunning bolt of light, and it poses a particular hazard to airplanes in flight. The average commercial aircraft is struck by lightning once every two years [*Fisher et al., 2004*].

Scientists have categorized lightning between the cloud and earth in terms of the sign of charge of the leader that initiates the discharge and named them Positive CG flash (PCG) and Negative CG flash (NCG) respectively. CG lightning has been studied more extensively than IC lightning. There are two main reasons. First is because of its practical interest. CG lightning is the cause of injuries and death, disturbances in power and communication systems, and the ignition of fires. The other reason CG lightning has been well studied is because lightning channels below cloud level are more easily photographed and studied with optical instruments [Uman,1987]. The goal of the LEFA project is to achieve a deeper understanding of individual lightning flashes and entire thunderstorms.

1.1.2 Background and Science Goals of LEFA

Recently, radio-based techniques have allowed unprecedented studies of IC lightning. Lightning mapping techniques based upon the measurements of lightning electric field in the radio frequency range have been applied to provide wonderful time-resolved pictures showing where lightning initiates and how lightning channels propagate inside thunderclouds. One of these techniques is used in the New Mexico Tech Lightning Mapping Array (LMA). However, these pictures only provide limited information on the main effect of lightning, which is to move electrical charge from one place to another along ionized plasma channels. In order to find the amounts of charge moved along the channels, past work included the development of field-change meters (also called slow antennae) for applications on the surface of Earth [Krehbiel *et al.*, 1979] and on balloons [Sonnenfeld *et al.*, 2006] to follow the rapid changes in electric field during lightning flashes.

Balloon-borne instruments have recorded changes in the electric field vector. They flew into thunderstorms in the vicinity of Langmuir Laboratory in central New Mexico. In the data analysis, the LMA around the Laboratory constrained the

location of the charges so that the amounts of charge transported by lightning could be deduced from the electric field measurements at the balloon. Special mathematical techniques were developed in order to combine the geometrical information from the LMA with the electrical information from the balloon-borne sensors. The mathematical analysis from these first flights made it clear that only the charges nearest the balloon instrument could be determined with adequate precision. To better locate these and the more distant charges as they are transported by the lightning channel, LEFA network makes E-field measurements at a number of additional locations spread over tens of kilometers.

The LEFA is a network of broadband electric field sensors, also called field-change meter (FC meter), deployed in the vicinity of Langmuir Laboratory's radio-frequency LMA network. Through the LEFA project, improved understanding of thunderstorm electrification and electrical dynamics of charge motion in a thunderstorm will be obtained. The measurements acquired through the LEFA will be interpreted with recently developed mathematical inversion algorithms. The combinations of the results from two sensor networks, i.e., the LEFA network, and the LMA network, could provide a map of charge transport in the entire region of a thunderstorm. With the results from the analysis of LEFA measurements, charge-flows and currents, as important factors in connection with lightning damages to facilities on the ground [*Hager and Sonnenfeld, 2007*], are going to be able to be determined. Also, results of case studies of charge transfer in individual lightning discharges could be integrated into dynamic cloud models, yielding a complete scenario of the micro-physics and transport of particles in a thundercloud along with the neutralization of charge by lightning. Learning about the charge structure might aid in predicting if and where lightning will occur.

1.2 Organization of the Thesis

At the time of this writing, the LEFA network is still under construction, but six complete salad-bowl slow antenna stations have been set up. (The sensor plates and analog board are integrated into a stainless steel salad-bowl, so the instrument is also called salad-bowl slow antenna.) This thesis began with introduction of scientific and design requirements of LEFA network and the details of the slow antenna station, which consists of the FC meter, the solar power module, the data acquisition module and the wireless communication module, as well as how it satisfies design requirements in Chapter 2. A ground-based instrument (the salad-bowl slow antenna) to detect the rapid variations of the electric field resulting from lightning flashes will be introduced specifically because it is critical in the LEFA. Chapter 3 presents the initial calibration site of relative gain ratio between different channels of one station, referring to self-calibration, and different stations, referring to cross-calibration, then details of calibration procedure, and results discussion. Chapter 4 presents the exciting initial results obtained when six fully-functioning stations were deployed in the field and a large frontal storm passed over the state of New Mexico. The wealth of data obtained from the October 20, 2009 storm allowed a first field cross-calibration of the instrument sensitivities and allowed us to study the effect of distance of the flash from the station on field-intensity. Also in Chapter 4 we present simple multi-station analysis of a CG and IC flash and show that they differ in details that can be understood with basic concepts of how leaders and return-strokes operate.

CHAPTER 2 LEFA Requirements and Summary

This chapter begins with introduction of scientific and design requirements for LEFA. Next the detailed design of a single station is covered. A station comprises an FC meter, a GPS unit, data acquisition, solar power, and networking modules, each of which will be discussed. Finally, the current LEFA configuration is described.

2.1 Requirements of LEFA

Slow antenna

The field-change (FC) meter (sometimes called a delta-E meter or slow antenna) is a device with a long history in atmospheric electricity research [*Chalmers*, 1967]. Typically, they measure changes in electric field that occur over periods less than a second and as short as tens of microseconds. Slow antennae differ from field-mills in this regard, which measure changes that occur on the scales of hours and minutes and as short as 0.1 second.

The frequency range selected makes slow antennae relatively insensitive to the slow processes of cloud charging which are covered by field mills, but quite sensitive to the effects of lightning itself. Bruce, and then Uman, separated effects of the lightning return stroke observed at the ground level into “electrostatic, inductive and radiation” [*Bruce*, 1941, *Uman*, 1987]. The time-scale of a slow antenna encompasses well all electrostatic effects, and, depending on the low-pass time-constant selected, begins to notice some of the inductive effects. In the modern understanding of lightning, it is realized that radiation effects accompany the initial breakdown of air leading to a conductive channel, while the inductive and electrostatic effects represent current flow and charge transport, respectively. The electrostatic effects are relatively slow. The peak current of a return stroke lasts for

20 μs (median value). If data are sampled more slowly than that, primarily electrostatic effects will be observed. Since charge transport is our primary interest, the 20 μs sampling period selected is appropriate, though some inductive effects can still be seen. There have certainly been studies that used shorter time scales [e.g., *Shao et al.*, 2006], but instrument complexity, cost and data handling problems increase with bandwidth, so this project is focused primarily on what can be learned from studying electrostatic and inductive phenomena.

Three channel design

For any measurement made on the ground, the effect of the ground plane itself is substantial. Whereas a charge suddenly created (or discharged) in free-space has a field that falls off as $1/r^2$, the inclusion of the ground plane and its image charge means the fundamental distance dependence is $1/r^3$. The dimensions of a storm can range to the tens of kilometers, so the new instrument is expected to be useful over this same range of distances. If considering a charge that is only 300 m distant vs. one that is 30 km distant, a factor of 100 difference in distance corresponds to a factor of one million in predicted field-change. This means the FC meter must have a very large dynamic range. Likewise, a flash that comes to ground near an instrument or a channel that passes directly overhead is likely to be very interesting; so flashes that are close should be detected without saturating the instrument.

Multi-station measurement

A single station measurement of electric field change can clearly see the dramatic feature of a lightning return stroke. For flashes that occur close to the station, it may see the approaching lightning leader, as well as small changes that occur after the return stroke (also called “K-changes”). The preceding sentences are specific to cloud-to-ground (CG) lightning flashes. A single-station can also see field-changes that occur due to intracloud (IC) flashes. IC flashes typically do not exhibit the dramatic and sharp feature of a lightning return stroke. Despite the rich complexity of wave-forms observed, progress in these studies has been hampered by the difficulty

of interpreting the data obtained. On PCG flashes, the sharp return stroke feature may be hard to see [Krehbiel, 1981]. In this case a single station measurement may simply be unable to discriminate an IC from a CG flash.

Multi-station measurements have some advantages in data interpretation over single-station measurements. It is relatively easy to distinguish IC flash, or the IC part of a CG flash by looking at results from multiple stations. Further, it is easier to separate out noise and other parasitic effects local to a single station by looking only at effects that correlate between multiple stations. If one has four or more stations, one can interpret a return stroke and measure the location in x , y , and z of the centroid of charge transported to ground, as well as the charge Q transported. If one has seven or more stations, one can interpret an IC flash with a dipole model. There are seven unknowns in a dipole model of an IC flash. They are: the transported charge Q , the point from which the charge is extracted (x_1, y_1, z_1), and the point where the charge is deposited (x_2, y_2, z_2). Seven stations mean one has seven equations and can solve for seven parameters. With still more stations, the least-squares techniques can be used to improve the accuracy of fits, as well as fitting more complex charge distributions.

Actually a lightning flash is neither a monopole nor a dipole. While the LEFA only captures the effects of charge motion, it can be collocated with LMA, an instrument that measures the location of the channels in the sky as they are created. By combining the two instruments, one can hope to see the charge motion of lightning in considerably more details than monopoles and dipoles. Sonnenfeld, Winn, Lu and Hager have already had some success in these efforts by combining balloon measurements with LMA [Hager *et al.*, 2007, 2009].

While single station measurements of field-change are relatively commonplace, multi-station measurements are less so. The LEFA updates the pioneering work of Krehbiel *et al.* [1979] with new technology. Other well-known multi-station

measurements are the Los Alamos Sferic Array (LASA) [Shao *et al.*, 2006], though this concentrates on frequencies to 500 MHz, the World Wide Lightning Location Network (WWLLN) [Lay *et al.*, 2004], which limits itself to low frequencies, and the U.S. National Lightning Detection Network (NLDN) [Cummins *et al.*, 1998], which primarily measures magnetic rather than electric fields. In contrast to these other instruments, the LEFA concentrates on making broadband low-noise measurements at frequencies between 6 Hz and 25 kHz.

These scientific requirements devolve to design requirements as follow:

1a) Need a 50 kilo-Sample/sec (kS/sec) sustained data rate. This encompasses the range of time-scales encompassed by the electrostatic processes in lightning. The data rate should be sustained because it is not necessarily obvious how to do a good real-time trigger that does not miss any part of a flash, particularly for distant flashes which can be of interest or for the IC processes that precede the CG flashes. This also leads to requirement 1b.

1b) Need a way to manage 24 Mbytes/minute of data. This is unavoidably what you get when you sample 200 kS/sec at two-bytes/sample.

2a) Need a 20,000,000:1 dynamic range. This allows observing flashes over a range 272:1 in distance from the instruments (assuming a $1/r^3$ dependence of field on distance). This also leads to requirement 2b.

2b) Need the instruments to operate in the typical environment of thunderstorms.

3a) Need a network of instruments spreading over 30 km. This encompasses the typical extent of a lightning flash, and leads to requirements 3b and 3c.

3b) Operate instruments for an entire storm season at remote locations without local power or cabled network connections. This necessitates solar operation and low-power design. This allows operation in the vicinity of Langmuir Laboratory,

and for practical issues such as using land that is available and far from sources of interference like power lines.

3c) Need a way to check proper operation and control remotely. This is a practical matter to assure that a large number of complex instruments are all operating properly on short notice before an active storm.

4) Maintain sub-sample accurate time between all stations of the network. This allows inter-station correlation and correlation with LMA.

The current LEFA network satisfies all above design requirements.

2.2 Overview of a LEFA Station

The data acquisition part of each LEFA station is built around a single board computer called a “puma” by its manufacturer. LEFA networking software communicates with this “puma board” by name and number (puma2, puma4, etc). Thus we have gotten in the habit of saying “puma2” to refer to LEFA station because it is shorter. Thus when you see a reference to puma2, puma5, etc., in what follow, it is a reference to an entire station, not just a single computer board.

Figure 2.1 is a picture of a salad-bowl slow antenna (Station puma6). A complete station is composed of field-change meter, data acquisition module (DAM), wireless communications, and solar power sections and GPS unit. In Figure 2.1, the field-change meter is the inverted bowl on a stand and the data acquisition module is beneath the white plastic box (which protects from rain and reflects heat). The wireless antenna and solar panels are clearly visible. The white box under the solar panels contains batteries to support the instrument when sun is inadequate. The GPS unit is the small black box sitting on a brick on top of the white data-acquisition housing.

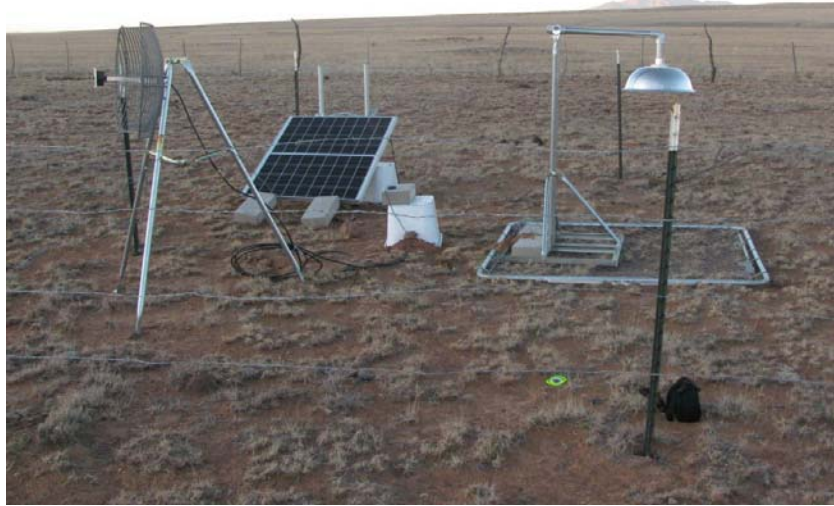


Figure 2.1 Picture of Station Puma6 Deployed in k2-EMRTC

Figure 2.2 provides a block diagram including the main connections between the major subsystems of a station. The data acquisition module is enclosed in an aluminum box, and is surrounded by a dotted-line box in Figure 2.2. Most of the DAM functionality is itself contained in a stack of three PC-104 circuit boards which are indicated by a smaller box inside the DAM module. These circuit boards are: a SBC (the puma), a 200 kSample/sec A/D (the fast A/D), and a 10 Sample/sec A/D (the slow A/D). Figure 2.2 shows the analog signal from the FC meter is low-pass filtered at a signal conditioning board (filter board) before running to the fast A/D, thence the computer and the hard-drive. The GPS signals (serial port and PPS) are combined at the TX/PPS signal conditioner and also run to the fast A/D. Slowly varying signals (temperatures, battery voltages, and future field-mill data) are routed to the slow A/D. Power requirements of various modules are indicated by dashed and dash-dotted lines in Figure 2.2.

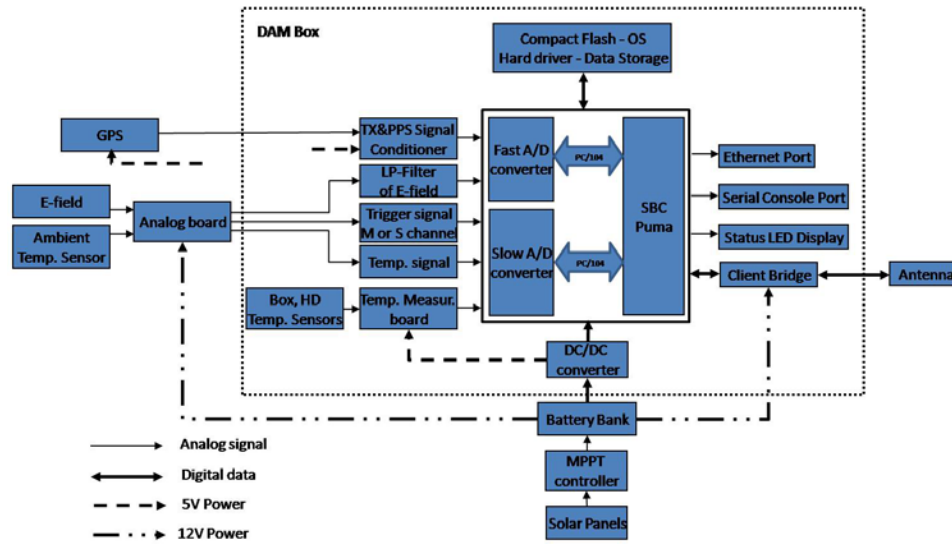


Figure 2.2 Slow Antenna Station Block Diagram

Having introduced the overall system integration plan, the remainder of this chapter is dedicated to a more detailed discussion of how many of the hardware modules work and how they satisfy the design requirements outlined in section 2.1. Since the primary subject of this thesis was the calibration of the entire LEFA network, the details of the analog sensors (the FC meter) will be focused firstly (and fairly heavily) on.

2.3 Field-Change Meter

The field-change meter is composed of the newly developed salad-bowl slow antenna, a meter stand and a metallic mesh. The salad-bowl slow antenna contains three separate electric field sensors for determining how lightning activities alter the ambient E-field vector, which near the ground is perpendicular to the ground surface due to the image effect of the earth. It also contains an analog board for converting the *E*-field to a voltage signal. Because the real ground is not a perfect conductor, the ground mesh is used to make sure the surface of the earth directly under the sensor

plates is uniform and equipotential. That satisfies the premise of the image effect. The ground mesh is a steel yard gate and will behave like a perfect conductor. The meter stand is used to support the instrument salad bowl. The stand must be considered to be a part of the instrument, thus all the stands are made with the identical design. (Remaining confusion about differences in stand design made it hard to understand the cross-calibration results, as will be seen in Chapter 3.)

2.3.1 Mechanical Design of Slow Antenna Sensor

Multiple channels with different gains allow a slow antenna to measure electric field changes over a large range without being saturated by lightning discharges that occur close to the antenna and missing the lightning that occur far away the antenna. Figure 2.3 shows the mechanical design of the sensor. The “salad-bowl” is a 14.4-cm high hemisphere of 24-cm radius stamped from a 0.3-mm-thick stainless steel. The sensing area is divided into three electrodes that are connected individually to dedicated amplifiers with different gains. The small central circular disc region of the sensing plate is called the “insensitive” channel because it has the smallest sensing area and the lowest electronic gain of all the three channels. The middle circular ring is called the “medium” channel since it has a medium sized sensing area and a gain set between the gain levels of the other two sensors. The outer ring, the electrode of the “sensitive” channel, has the largest sensing area and the highest gain. The circular plates of both the “medium” and the “sensitive” channels are made of 0.3-cm-thick aluminum plates, while the sensing plate of the “insensitive” channel is a nickel plated copper film integrated onto a printed circuit board (PCB). This PCB is also called the analog board.

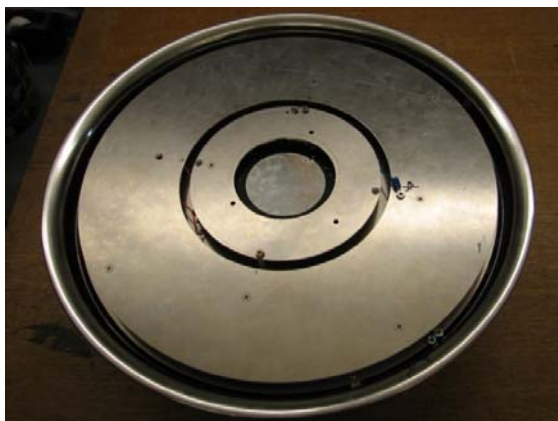


Figure 2.3 Photo of Sensing Plates Installed on Salad-bowl Slow Antenna

The sensing area is divided into three sections. The central plate is connected to the insensitive channel. The smaller and the larger ring plates are connected to the medium and the sensitive channels, respectively. Gaps are left to satisfy the requirement of operating in the environment typical of thunderstorms, so that raindrops will not span gaps between electrodes.

2.3.2 Analysis of Circuit of Slow Antenna

Appendix A shows the detailed circuits of version B of the salad-bowl slow antenna, which is composed of three-channel circuits, trigger circuit, temperature sensor and output connector. It is easy to see that these three channels have similar circuits. Each channel has a charge amplifier at the input stage, followed by voltage amplifier at the gain stage. According to the physical E-field sign convention, the positive output voltage of the charge amplifier corresponds to a positive E-field, while the gain amplifier is an inverting amplifier. Therefore, a negative output voltage of the whole circuit represents a positive E-field.

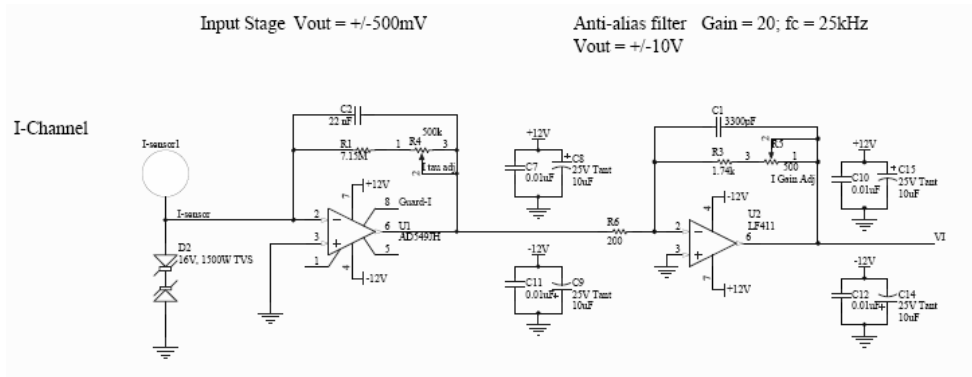


Figure 2.4 Schematic of the I-Channel in Salad-bowl Slow Antenna

2.3.2.1 Component Selection Criteria

Figure 2.4 shows the schematic of I-Channel in slow antenna. The ultralow input bias current operational amplifier (op amp) AD549JH from Analog Devices is chosen as a charge amplifier. The open loop frequency response of AD549JH shows that when the frequency of input signal is smaller than 100 kHz, the open loop gain remains constant at 90 dB. Additionally, according to the data sheet, the AD549JH is in a TO-99 hermetic package, and the case is connected to Pin 8 so that the metal case can be independently connected to a point at the same potential as the input terminals, minimizing stray leakage to the case. This is important as the instrument is often operated in a wet environment where surface leakage currents may be substantial. The op amp LF411 is used as a voltage amplifier, which magnifies the output voltage from the charge amplifier by a factor of about 20. A lightning return stroke may occur in 1 μ s, and may drive the output of the LF411 to full scale (10 V), thus a slew rate of 10 V/ μ s is required on the second stage, whereas a rate of 10 V/ μ s/Gain = 1.0 V/ μ s is required on the first stage of the insensitive channel and its gain is 10. Generally, since the bandwidth is less than 1 MHz, it will never reach these slew rates, but it is good to have design margin. Some fundamental parameters regarding AD549JH and LF411 are listed in Table 2.1, showing that they satisfy the requirements for high slew-rate and low leakage current previously discussed.

Parameter	AD549JH	LF411	Units
Input Impedance (Common Mode)	$10^{15} / 0.8$	10^{12}	Ω / pF
Open-loop Gain	10^6	2×10^5	V/V
Slew rate	3	10	V/ μ s

Table 2.1 Parameters of the Operational Amplifiers, AD549JH and LF411

2.3.2.2 Circuit Analysis

This analysis begins with the principle of a traditional slow antenna [e.g., *Krehbiel et al.*, 1979]. The schematic diagram in Figure 2.5 documents the simple slow antenna, which only contains one charge amplifier. The electrode, also called the sensor plate, is connected to an integrating operational amplifier. It measures the changes of the charge induced on the surface of electrode by the change of the atmospheric electric field, which is caused by the lightning flash. The ambient electric field to be measured is usually assumed to be uniform. However, due to the presence of the electrode, this electric field is distorted and its actual distribution becomes non-uniform on the surface of electrode. In order to overcome this problem, the effective area of electrode, A_{eff} , is introduced to associate the change of E-field (ΔE) to be measured with the charge changes (ΔQ) induced on the electrode as

$$\Delta Q = \varepsilon \cdot A_{eff} \cdot \Delta E \quad (2.1)$$

where $\varepsilon \approx \varepsilon_0 = 8.854 \times 10^{-12}$ F/m is the permittivity of air. Equation 2.1 is derived from Gauss's Law, which leads to the basic formula of surface charge distribution

$$E = \sigma / \varepsilon \quad (2.2)$$

where the mean surface charge density is calculated as $\sigma = Q/A_{eff}$.

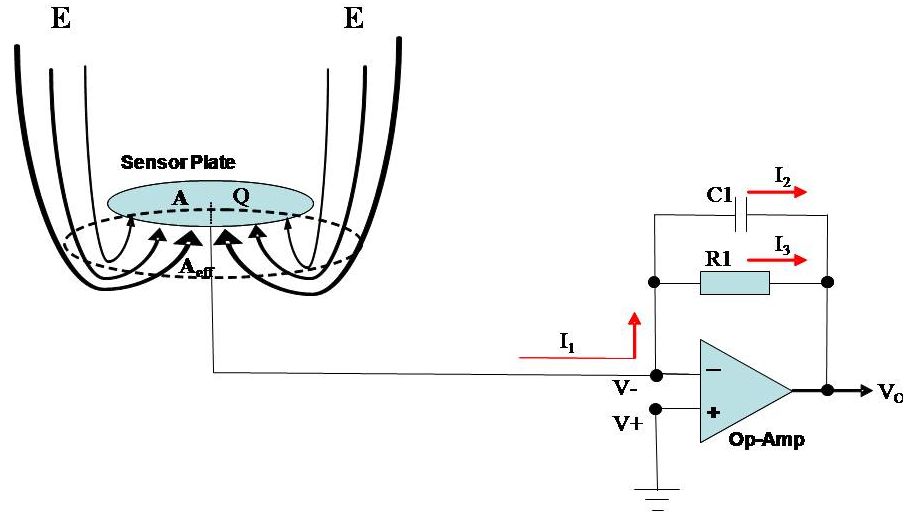


Figure 2.5 Simplified Schematic Diagram of the Circuit of a Slow Antenna

What operational amplifiers do should be clarified here. An integrated circuit op amp amplifies the voltage difference $V_+ - V_-$ between its '+' and '-' inputs (see Figure 2.5), the output voltage is $V_o = A(V_+ - V_-)$, where A is the open-loop voltage gain of the amplifier. Two properties of op amp make them particularly useful: 1> The open-loop voltage gain A is large, typically 10^5 at low frequencies. 2> The internal resistance between the + and - inputs is large, typically $10 \text{ M}\Omega$ for operational amplifiers which use bipolar junction transistors (BJT), and 10^{10} or higher for operational amplifiers (like the AD549JH) which use field effect transistors (FET). Operational amplifiers are used by providing negative feedback (usually resistance) from the output to the - input, which substantially reduces their gain. When the open-loop gain A is much greater than its close-loop gain, then the voltages, V_+ and V_- , are very nearly equal. Furthermore, when the resistance used in the feedback loop is small compared with the internal resistance of the operational amplifier, then the currents into the + and - inputs can be neglected. When these conditions are true the op amp is said to be ideal. An ideal op amp can be analyzed by adding the following two simple rules to the usual rules for circuit analysis: 1> The + and - inputs are at the same potential. 2> No current flows into either input. For an ideal operational amplifier, the gain depends only on the feedback elements and not on its open-loop

gain A nor on its internal resistance.

As Table 2.1 shown, the open-loop voltage gain A of the amplifier AD549JH is 10^6 and its internal resistance is $10^{15} \Omega$. Figure 2.4 shows the maximum output of the amplifier AD549JH V_o is 500 mV, so the voltage difference between the + and – inputs ($V_+ - V_-$) will be $0.5 \mu V$, and it is very small. Also the leakage current should be $0.5 \cdot 10^{-6} V / 10^{15} \Omega = 0.5 \cdot 10^{-21} A$ and it is very trivial. Two above conditions are true for the amplifier AD549JH, so it can be said to be ideal.

Therefore, two key principles clarify operation of AD549JH. 1) Because there is no flow into the op amp, the current from electrode must go through the capacitor C_1 and resistor R_1 . This justifies using Kirchoff's current law on the V_- node of the circuit in Equation 2.3. 2) One leg of feedback loop is held at ground potential (0 V). Because the main job of the ideal op amp is to adjust the output such that the inverting input equals the non-inverting input. And, since the non-inverting input is at ground (0 V), the inverting input along with feedback loop will be held at 0 V, too. The analysis of the circuit shown in Figure 2.5 gives equations as follows,

$$\begin{cases} I_1 = I_2 + I_3 \\ V_+ = V_- = 0 \end{cases}, \text{ and } \begin{cases} I_1 = \frac{dQ}{dt} \\ I_2 = C_1 \frac{d(V_o - V_-)}{dt} \\ I_3 = \frac{V_o - V_-}{R_1} \end{cases} \quad (2.3)$$

From the equations above, the output voltage from this circuit can be written as,

$$\varepsilon A_{eff} \frac{dE}{dt} = \frac{1}{R_1} V_o + C_1 \frac{dV_o}{dt} \quad (2.4)$$

From Equation 2.4, notice that the charge amplifier only responds to the variation in

electric field E . To simplify the circuit for the purpose of discussion, the resistance is always set to a value in the order of $M\Omega$, in order to ignore the effect of the first term in right side. Then the output voltage simplifies to

$$\Delta V_o = \frac{\varepsilon A_{eff}}{C_1} \Delta E \quad (2.5)$$

This equation shows the basic relationship between the change in the electric field and the output voltage change. When the E-field is constant, no change happens, the output voltage V_o is zero. When the E-field changes on a time-scale short compared to $\tau = R_1 C_1$ (the time constant of the charge amplifier), V_o changes proportional to the lightning E-field. Therefore the Equation 2.5 can be rewritten to

$$V_o = \frac{\varepsilon A_{eff}}{C_1} E \quad (2.6)$$

Equation 2.6 shows the relationship between the output voltage and the lightning electric field.

Equation 2.6 is only accurate for a lightning flash, whose frequency is higher than the cut-off frequency $f_c = \frac{1}{\tau}$. Let's take a look at the response in the frequency domain for our instrument. For the time interval starting at $t = t_0$, the time-varying E is derived by solving the differential Equation 2.4, which gives

$$E(t) - E(t_0) = \frac{C_1}{\varepsilon A_{eff}} \left\{ \frac{1}{R_1 C_1} \int_{t_0}^t V_o(t') \cdot dt' + [V_o(t) - V_o(t_0)] \right\} \quad (2.7)$$

The Fourier transform of both sides of Equation 2.7 gives,

$$\varepsilon_0 A_{eff} \cdot j\omega \cdot E(j\omega) = \frac{1}{R_1} V_o(j\omega) + C_1 \cdot j\omega \cdot V_o(j\omega) \quad (2.8)$$

where $\omega = 2\pi f$. Rewrite Equation 2.8 to get,

$$\frac{V_o(j\omega)}{E(j\omega)} = \frac{j\omega\varepsilon_0 A_{eff}}{R_1^{-1} + j\omega C_1} = \frac{j\omega\varepsilon_0 A_{eff} R_1}{1 + j\omega\tau} \quad (2.9)$$

Table 2.2 provides time constants of three charge amplifiers of version B design.

Channel	R_1 (M Ω)	C_1 (nF)	Time constant (s) ($\tau = R_1 C_1$)
Insensitive	7.15	22	0.157
Medium	25	6.2	0.155
Sensitive	132.15	1.2	0.159

Table 2.2 Time Constants of Three Charge Amplifiers of Version B Design

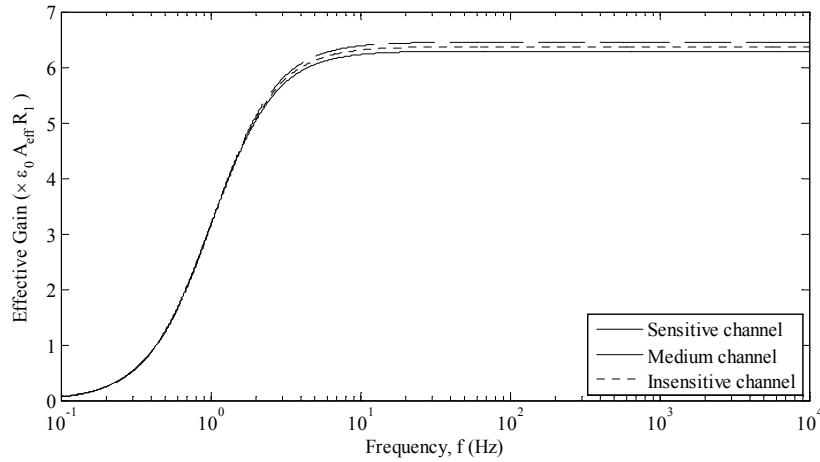


Figure 2.6 Frequency Responses of Three Channels for Version B Design

Figure 2.6 is a plot of Equation 2.9 for the value of RC used. It shows the frequency response is flat for $f > 6$ Hz. The charge amplifier also functions as a

High-Pass filter.

Equation 2.7 indicates a method to retrieve the true E-field from measured V_o for times longer than $\tau = R_1C_1$ when Equation 2.6 is not valid. This procedure is called dedrooping. Because the $1/(R_1C_1)$ factor appears as a “gain” in the dedrooping, it is helpful to design a circuit for which time constant τ is the same for all channels. The reason for a dedrooping process is also shown in Figure 2.7. The solid line is the change of E-field to be measured and it is simulated as a step function in this demonstration. While because of the existence of a resistor in the feedback circuit, the output voltage immediately begins to relax after the step change, as indicated by a dash line in Figure 2.7. The process is called relaxation. The dedrooping process, as an opposite process to relaxation, retrieves the voltage signal that is not affected by the relaxation.

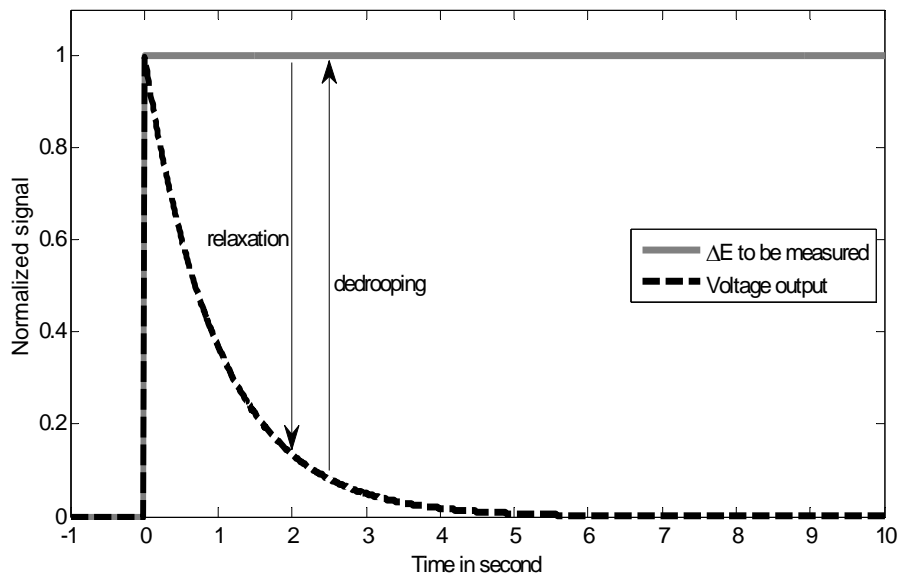


Figure 2.7 Relaxation and Dedrooping Processes

In the schematic of Appendix A, a lightning protection circuit is added in the input stage. It consists of two reverse serial Zener diodes. The circuit is designed

to prevent large voltages from damaging the circuits further down stream.

After the charge amplifier is a gain stage amplifier, which also functions as a Low-Pass filter to remove high frequency noise. The cut-off frequency of this analog design is 25 kHz. It is set by the Nyquist criterion for the fast A/D converter. Since the sampling rate is 50 kHz, the low pass is centered at 25 kHz to prevent aliasing in the data. A two-stage design is chosen to reduce the demands on each stage and to clearly separate the high pass or low pass functions of each stage. Also, the voltage amplifier on second stage is calibrated with a variable resistor to keep overall sensitivity of circuit boards constant to 0.1% for all analog boards. The gains of both the medium channel and the sensitive channel are set to -20. In version B of analog board, the gain of insensitive channel changes to -10 in order to make it less sensitive, compared to gain -20 in version A design of Appendix B. From Equation 2.6, the final voltage is

$$V_{out} = -G \frac{\varepsilon A_{eff}}{C_1} E \quad (2.10)$$

where G is the gain of the second stage. This relationship between the lightning E-field and the total output voltage is correct only for such lightning flash with frequency between 6 Hz and 25 kHz. In the design, the full-scale of total output voltage is ± 10 V, allowing to solve for the expected maximum lightning E-field which can be measured in each of the three channels, shown in the following table. It should be emphasized that the fields in column 5 of Table 2.3 are the fields as measured at the surface of each sensor plate. The field at the ground away from the distorting effects of the FC meter, which is actual quantity of interest, is considerably lower than these fields. Based on the calibration of the E-100 field mill, which is geometrically similar to this FC meter, the actual fields are likely about seven times lower than shown in Table 2.3. An absolute calibration of the FC meter is beyond the scope of this thesis.

Channel	Gain	Area (m ²)	C ₁ (nF)	$E_{\max} = -V_{out} C_1 / (\epsilon G A_{eff})$ (kV/m)
Insensitive	-10	0.005	22	496
Medium	-20	0.02	6.2	17.506
Sensitive	-20	0.1	1.2	0.678

Table 2.3 Theoretical Maximum of E-field Measured in Each of Three Channels

It is a challenge to log data effectively for an entire summer because of the limited data storage space. It would thus be helpful to have a trigger program that starts data acquisition only when lightning is detected nearby to at least one instrument. To enable this function, the analog board outputs a trigger signal scaled to be analyzed by the slow A/D board. To do this, a trigger program is run in SBC that can start the data acquisition program when the electric field change is bigger than a threshold value, currently set to +/-2 V. That is why to fetch a trigger signal from the analog board. As shown in Appendix A, the trigger circuit can fetch the output voltage of the M channel or S channel (using a jumper), and feed it to a slow A/D card. The output range of three channels is from -10 V to +10 V, while the slow A/D card only accepts the signal from 0 V to 10V. So an adder of +10V is used to get the signal with range from 0 V to 20 V, and then the 2X divider is applied to get a signal in the range that the slow A/D can accept.

The schematic of Appendix A also shows an additional feature. It is a temperature sensor. A National Semiconductor LM335M in 8-Pin SOIC surface mount package (SOIC is the abbreviation of Small Outline Integrated Circuit Package) was used. Such a precision temperature sensor has a breakdown voltage directly proportional to absolute temperature at +10mV/°C and has a linear output. It operates from -40°C to 100°C.

2.4 GPS unit

The GPS device is an essential part of the salad-bowl slow antenna station. Its primary purpose is to provide a time reference for the field-change data. The GPS signals including Pulse-Per-Second (PPS) signal and serial transmit (TX) signal are sampled by the fast A/D converter at 50 kHz interleaved with the other channels. It allows for aligning the E-field data of multiple stations with the Coordinated Universal Time (UTC), which is extracted from TX signal, to the nearest 20 microsecond. It is very important to know the exact time when some lightning flash happens so that the E-field data from our LEFA system can be correlated with the LMA data. The GPS also provides position information. The position information contains latitude, longitude and altitude of each station. The accurate position of each measurement station is needed to locate the charge centers discharged by the lightning in the subsequent data analysis.

The Garmin GPS35-LVS is a complete GPS receiver, including an embedded antenna. As shown in the center of Figure 2.2, the GPS is placed on the cement brick on top of the white cover, so that its antenna will have the maximum view of the sky. The GPS case is made of waterplastic plastic that can withstand the rugged operating conditions of a storm. The GPS is connected to the data acquisition module through a five-pin bulkhead connector. Appendix C Table C.3 shows the connector configuration for GPS. A list of device specifications is shown in Table 2.4.

The GPS unit is programmed to generate one type of output string, NMEA GPGGA, to the Data Acquisition Module. The data acquisition program `stx104_daq` and binary file process program `process_bin_file` use the NMEA GPGGA string to extract the time information. All other strings are turned off and the GPS unit is also programmed to enable its pulse per second output.

Weight	124.5 g
Size	56.64 mm x 96.42 mm x 26.60 mm
Operating temperature	-30°C to +85°C
Input Voltage	+3.6VDC to 6.0VDC
Input Current	120 mA typical 140 mA max
Satellite Tracking	12 or up to 11 with PPS active
Position Update Rate	1 sec.
Acquisition Time	45 sec. cold to 5 min. sky search
Position Accuracy	15 meters RMS
PPS Accuracy	+/-1 us at rising edge of PPS pulse
Interface	RS-232 compatible at 4800 baud
Data Format	NMEA 0183 Version 2.0 ASCII output

Table 2.4 Garmin GPS35-LVS Specification

2.5 Data Acquisition Module

2.5.1 Hardware

The Data Acquisition Module (DAM) is shown in Figure 2.8. The SBC, two A/D converters and 160G HDD implements the heart of the DAM. They are located in an aluminum box 360 mm L × 240 mm W × 120 mm H (Hammond Manufacturing). This Hammond box serves to shield the data-acquisition device from the EMI of the ambient environment. Further it provides a watertight and rigid platform to keep the electrical connections stable in the field. In order to ease assembly and repair, all parts are mounted on the aluminum base plate, as shown in Figure 2.9. Waterproof connectors are deployed in the front panel shown in Figure 2.10. Different connectors were used for each function to prevent connection mistakes in the field.

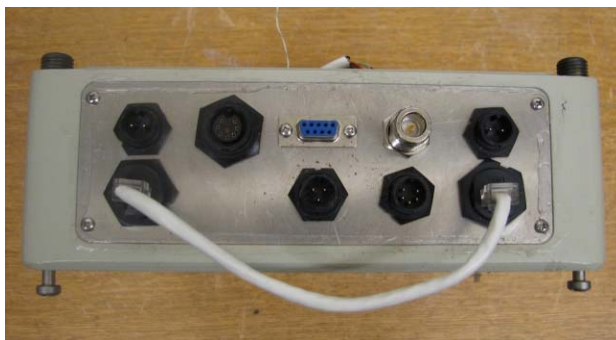


Figure 2.10 Picture of Front Panel

2.5.2 Sampling Resolution and Sampling Frequency

2.5.2.1 Fast A/D Converter

The Fast A/D converter has a 16-bit resolution and is programmed to measure the voltage range from -10 V to $+10\text{ V}$. Therefore, the data resolution in terms of voltage is $\sim 305\text{ }\mu\text{V}$. Using Equation (2.10), the minimum E-field resolution is 0.021 V/m on the sensitive channel.

The maximum aggregated sampling rate of the system is 200 kilo-Sample/sec (kS/sec). The STX-104 specifications claim the board is capable of a sustained 200 kS/sec data acquisition rate, and this is in fact the rate that is sustained without error in working LEFA stations for hours at a time.

This sampling rate is divided equally between four channels, which we designate channels zero, one, two, and three. The sampling rate for each channel is thus 50 kS/sec. Channels one, two and three digitize the insensitive, medium, and sensitive field-change signals. Channel zero digitizes the GPS signal, which is preconditioned as discussed next. The GPS outputs two needed signals on different wires. One output is the TX output, which encodes position and time information as an ASCII

string. The other is the PPS output. Figure 2.11 is a timing diagram for the two signals. The TX signal appears as a solid black pulse at the coarse time scale of Figure 2.11 because of the many data bits packed into each burst. Observation shows the PPS is never high during the TX transmission time. This suggests that the signals can be combined by an XOR circuit. The circuit we use to combine the TX and PPS signals from the GPS onto a signal wire for digitization is shown on Figure 2.12.

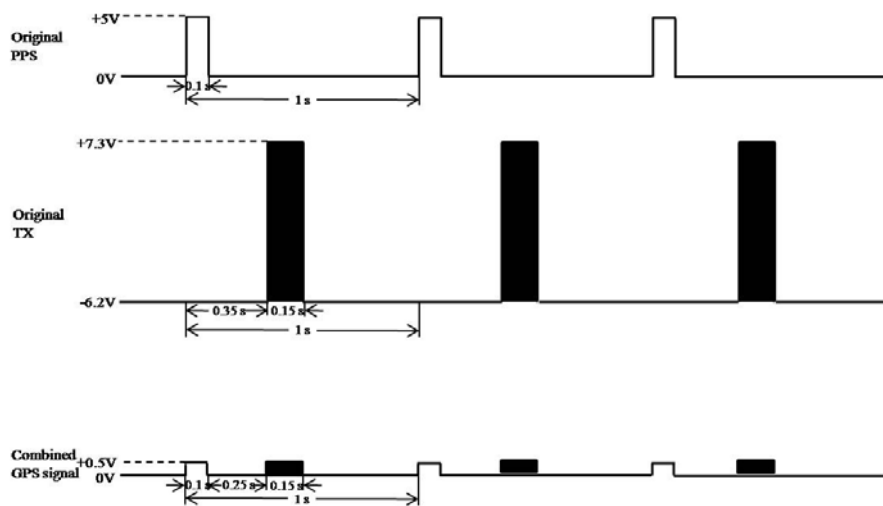


Figure 2.11 Sketch of the GPS Signal Conditioning Procedure

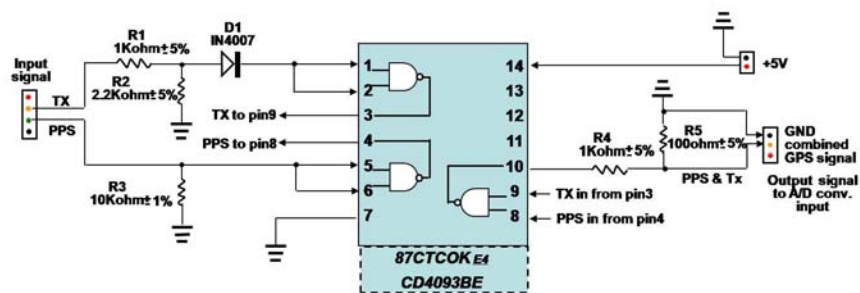


Figure 2.12 Schematic of the GPS Signal Conditioning Board (GPB)

2.5.2.2 Slow A/D Converter

The Analog-to-Digital converter of SAD card has 12-bit resolution and samples an input voltage from 0 V to 10 V. The minimum voltage resolution is therefore ~2.44 mV. It is tasked to record the information regarding the status of the station. In the first stage of deployment, SAD only records the trigger signal, temperature sensors, and battery bank voltage. When the LEFA is fully developed, electric field-mill will also plug into the slow A/D.

2.5.3 Noise Reduction

Laboratory test of the field-change board by Keith Morris yielded an output noise in the mV range. However, after studying the performance of systems deployed in the field, tens of mV of noise were observed in our digital data. After experimentation, Jeff Lapierre and Richard Sonnenfeld realized that the signal cables themselves (which were 25 to 50 feet long) were acting as antennae and adding MHz noise at the data acquisition inputs. Some of these MHz signals were aliased into the digitized data. The problem was solved by shortening the cables and adding a filter. Figure 2.13 shows the schematic of the filter board. The board is used to implement low-pass filters with $f_c = 1/(2\pi RC) \approx 106$ Hz cut-off frequency in each channel of the slow antenna. Note that there are resistors on both the “signal” and “common” leg of the filter. Because the fast A/D converter operates in differential mode, noise can couple in on either wire. Only the common-mode noise is digitized. Thus it makes sense to design a symmetrical filter, as shown in Figure 2.13.

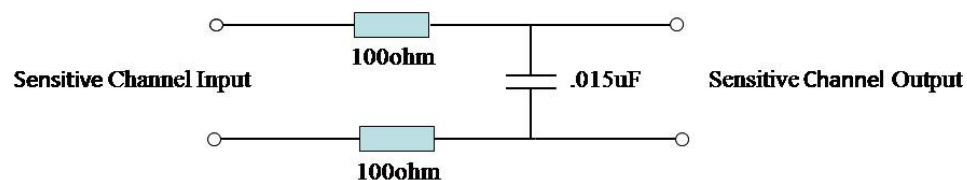


Figure 2.13 Schematic of the filter board

2.5.4 Data Acquisition Programs

The main reasons to use a Linux based distribution are Linux's open source nature, reliability, low cost, and good network performance. The Debian Linux distribution is chosen for the LEFA project because it is very common and easy to use without a GUI, which also means it has a relatively small size that is appropriate for the 2 GB compact flash card. Also, the Debian apt-get utility allowed for easily adding additional software packages and removing unneeded ones. One utility Ntpdate is counted on particularly. This package is used to synchronize the computer system to the NTP (Network time protocol) server of Langmuir network. Ntpdate runs on boot and sets computer time to a network reference.

There are two types of software, shown in Table 2.5 and 2.6 respectively. Table 2.5 lists the software that operates the data acquisition and the network.

Program	Function
<i>stx104_ai_file</i>	Operates the stx104 DAQ board, Takes data on 4 channels at 50 ksp/s, Streams data to disk.
<i>ts9700_aifile</i>	Operates TS9700 board, Takes 8 channels of slow data at 10X/second or less.
<i>trig_daq</i>	Launches <i>stx104_ai_file</i> in response to trigger conditions
<i>Watch-dog</i>	Looks for failures of three programs above and restart if they crash

Table 2.5 Software that Operates the Data Acquisition and the Network

Program *stx104_ai_file* generates binary files at a speed of ~24 Mb per minute so that it only takes four to five days to fill up the local 160GB hard drive. For this reason, the procedures are needed to implement to rapidly deal with the data in the field. Data management software is also implemented and listed in Table 2.6.

Program	Function
<i>filter_bin-2.4_hex.py</i>	Filter out useless data
<i>bin2bmp</i>	Image all data
<i>port_init</i>	Listen to the network, Receive the storm status and other commands
<i>datasync</i>	Automatically analyze and upload the data
<i>Status.py</i>	Report the instruments status to Web

Table 2.6 Data Management Software

During the post data analysis, the *process_bin_file* program is used to process the binary files generated by *stx104_ai_file*. It contains several python functions necessary for decoding the binary data, extracting time information, and writing data to a text or binary file. After *process_bin_file* is run, the properly time-stamped data can easily be further analyzed with MATLAB.

2.6 Network and Wireless Module

2.6.1 Network Operations

Wireless communications are critical to the smooth operation of the LEFA. The LEFA is designed to be tolerant of network outages, but operation is much easier if there is good network connectivity. Network connectivity is implemented via a standalone embedded access point, the CPU board WBD-111, which interfaces to a WMR-400 radio. The SBC connects to the radio with an Ethernet cable, and the radio handles all connectivity issues. IP addresses of all instruments are set to the 10.0.100.xxx subnet used by Langmuir Laboratory. From a network point of view, each instrument cannot tell whether it is sitting in a remote field location or a comfortable laboratory. All that varies between field and lab is the effective network bandwidth. The ability to run an instrument unmodified in the field or in the Lab

makes building, debugging and maintenance much simpler. When the network is operating, the following four functions are implemented:

1. Instrument Triggering
2. Status Reporting
3. Data Post-Processing
4. Data Upload

The instrument triggering function is the only critical function of the four listed above. If the instruments cannot be enabled, no data will be acquired. Because instruments take data for an hour after receiving a trigger, even a very intermittent network connection will allow this key function to operate.

Status reporting, post-processing, and data upload do require that the network be operating well. However, the local hard drive can store three days of continuous data, buying time to fix a network problem even if these functions fail completely. Furthermore, as outlined in the discussion of the field-change circuit board, the instruments have the capability to self-trigger data acquisition if the field change meter detects a field change over a settable threshold.

The network topology is shown in Figure 2.17. It has a multipoint-to-multipoint communication infrastructure and is connected by wireless access points attached with the central antennae. As shown in Figure 3.1, the antenna is a 2.4 GHz parabolic 19 dB gain antenna from Hyperlink. It is mounted 5 feet above ground on the steel mast supported by a tripod. This grid dish parabolic antenna is constructed of welded steel wires and comes with a 30 inches pigtail with N female connector. It is attached to the client bridge through the cable LMR-400 with N-male connectors. Still more detail on connectors and cables maybe found in Appendix C.

2.6.2 Power Control over the Network

The WBD-111 has an additional valuable function. It allows us to power the DAM off and on over the network. Figure 2.1 shows that power is connected to the WBD-111 so that it is always on, and a network connection to the bridge is always present. However, GPIO pin 6 of the WBD-111 is connected to the enable pin of the DC/DC converter that powers all of the DAM's 5-V logic. One can log onto the bridge and use the commands `gpio -w 6 0` and `gpio -w 6 1` to power the DAM off or on.

2.7 Test

After building the puma box, the test should be conducted to validate the functions and cable connectivity in the puma box. It is necessary to assure that DAM takes data successfully and has good wireless communication before the instruments are deployed in the field. Appendix D shows the test instruction and test form for DAM and wireless module.

2.8 Solar Power Module

The station must stay powered for a reasonable amount of time so that the instrument will be running especially when the thunderstorm is happening randomly, as well as be able to receive transmission from station to remote server every day. The goal was to have a system that would operate for at least three days without any sun, and that would have sufficient capacity to run for the entire summer on available sun without draining the batteries. Based on tests reported in Section 2.8.2, the solar power module could keep operating FC meter, data acquisition module and wireless communication for two months on the roof of Workman Center using plentiful solar

energy in New Mexico. It consists of two serial KC85T solar panels from Kyocera Co., an MPPT250 (Maximum Power Point Track) controller of BZ Products, Inc., five hermetically sealed threaded case filters and a battery bank of two parallel 12 V Blue-Top batteries from Optima Batteries Co. The filters are used to filter the electrical and magnetic interference (EMI) caused by the MPPT250 controller. Figure 2.14 shows the schematic of solar power module. As Figure 2.17 shows, the 12 V battery bank powers the FC meter and client bridge directly and it also provides 5 V power to the Puma SBC, GPS, GPS board and Temperature Measurement board through the PXD20-12S05 DC/DC converter of Lambda.

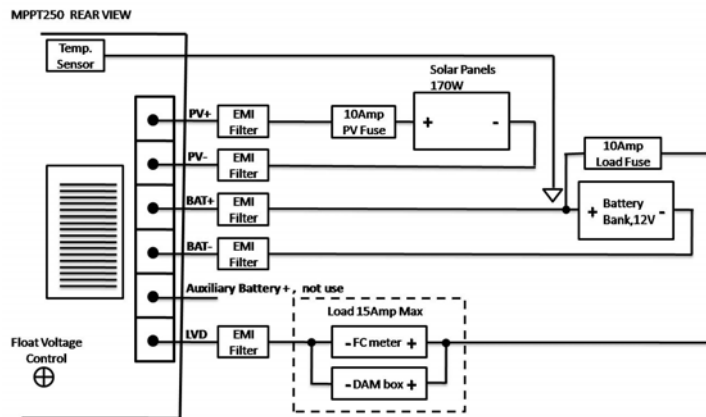


Figure 2.14 Schematic of Solar Power Module

2.8.1 Power Budget

Table 2.6 shows the salad-bowl slow antenna station theoretically consumes about 12.2 watts of 5 V power source and 9.9 watts of 12 V power source. The 12 V parts run directly from the battery bank, whereas the 5 V power is obtained from the DC/DC converter. The efficiency of PXD20-12S05 DC/DC converter is 87%. Solar power system needs to provide a total of $12.158/0.87+9.9 = 23.9$ watts power. The typical winter peak sun hours of Socorro, New Mexico are about 5 hours per day [2] and the efficiency of MPPT controller is approximately 90%. Therefore, the output

of two solar panels is about $2 \times 5h \times 85W \times 0.9 = 0.765 \text{ kW}\cdot\text{h}$. It is able to keep the station running 24 hours because our daily load is $25.275 \text{ W} \times 24 \text{ h} = 0.609 \text{ kW}\cdot\text{h}$. The thunderstorm season of Socorro county of New Mexico is June, July, August and September every year and always has more sun hours than the winter. Battery requirements are based on the daily load ($\text{kW}\cdot\text{h}$) and the recommended days of autonomy. The capacity of battery bank is $110 \text{ Ah} \times 12 \text{ V} = 1.32 \text{ kW}\cdot\text{h}$, which can run the station theoretically $1.320/0.609 = 2.2$ days. While referred to manufacturers specifications to give a conservative power consumption estimate, power consumption was measured. Total power consumption of the station (omitting the Field Mill) was measured to be $1.45 \text{ A} \times 12 \text{ V} = 17.4 \text{ W}$.

Voltage(V)	Part Name	Theoretical Power(W)
5	SBC	5
	Fast A/D board	1.875
	Slow A/D board	0.15
	Hard Disk Driver	5.5
	GPS	0.3
	GPS board	0.333
	Temp. board	0.375×10^{-3}
	Total	12.158
12	Field Mill	5
	Client Bridge	1.8
	MPPT controller	1.8
	Slow antenna	1.3
	Total	9.9

Table 2.7 Power Budget of Station

2.8.2 Performance of Solar Power System

In the previous section we determined that our instrument might need up to 25

Watts continuously to run. Though that is a conservative estimate, I tested whether the solar-power system we selected could provide 25-W of power continuously under field conditions. The bottom line result is that the selected solar panels and controller provided 25 Watts round the clock for the two month period of March and April, 2008. Details follow.

These tests were all performed before the first LEFA station existed. Thus, the load of a station was modeled with a high power 5 Ohm resistor (the "Load" in Figure 2.15) in series with a 1.25 Ohm resistor. At a nominal battery voltage of 12.5 V, a 6.25 Ohm resistor draws exactly 25 Watts.

The solar controller used was an MPPT-250 (illustrated in Figure 2.14) and the solar panels evaluated were a pair of BP-585s from BP Solar. BP585 specifications are shown in Table 2.8. (After obtaining a successful result on these tests, our project switched over to Kyocera KC-85 panels, which we believe to be substantially the same as the BP-585s.)

Data acquisition used a multi-channel HOBO data-logger. As shown in Figure 2.15, Ch. 1 of the Hobo was used to measure current through the load, while Ch. 3 measured voltage. Because the Hobo can only measure 0-2.5 V (at 10 mV resolution), voltage dividers were used for both channels to bring the 0-14 V battery voltage into range. Ch. 3 used a 1:21 voltage divider, making the least significant bit 210 mV. Ch. 1 had a voltage divider of $(16/43) \cdot (1.25/6.25) = 1:13.44$ and could measure current to a precision of 21.5 mA. The known voltage divider ratios were used to scale the voltages measured by the Hobo to generate the voltage and current plots in Figure 2.16. Power, shown in the third panel of 2.16, was not measured. Rather it was calculated as the product of Voltage and Current.

Figure 2.16 clearly demonstrates that the system was sustaining more than 25 Watts of power to the load. It also shows the diurnal variations of available power.

At night, clearly, the system was running on battery power. The location of the knees in the power curves, at roughly 9 am and 5 pm show that during the period of the test our system was getting about 8 hours of useful solar power each day.

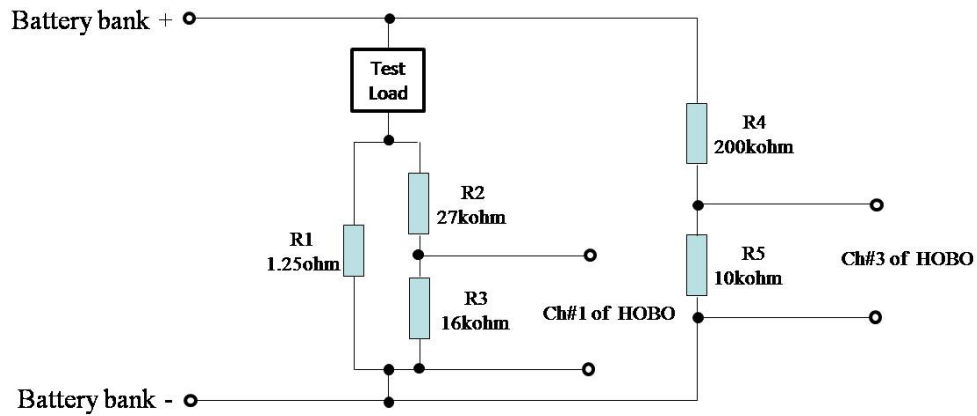


Figure 2.15 Schematic of Data Logger

Maximum power(P_{max})	85W
Voltage at P_{max}	18.0V
Current at P_{max}	4.72A
Warranted minimum P_{max}	80.8W
Short-circuit current	5.0A
Open-circuit voltage	22.1V

Table 2.8 Electrical Characteristics of BP 585 Module

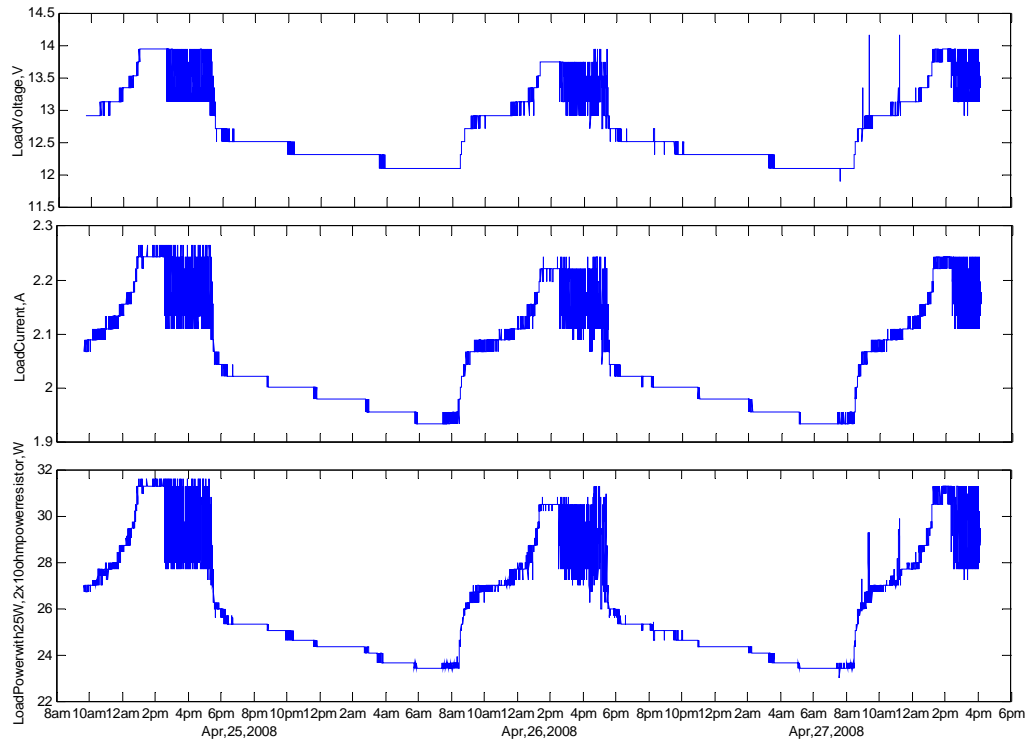


Figure 2.16 Performance of Solar Power Module

2.9 Current Configuration of the LEFA Network

The infrastructure of the current LEFA system is sketched in Figure 2.17. This system consists of two main components, the server subsystem and the network that comprises 16 sensor stations deployed over a roughly 30 km diameter region. For convenience, stations currently are named as Puma#, because the single board computer of DAM is Puma from Versalogue Corporation, shown in Table 2.9.

Station Name	Location
Puma2	Workman Center Roof (test)
Puma4	Pound Ranch (pilot)
Puma5	Six-Mile
Puma6	k2-EMRTC
Puma7	Balloon Hangar
Puma8	d3-EMRTC

Table 2.9 Station Names and Locations in Current LEFA Network

The server subsystem, which is also called the network management system, has two principal functions. The first function is to archive the lightning data, and the second is to remote control every station, including collecting system health information (for example, the CPU temperature of single board computer, local hard drive temperature, and battery voltage, etc.) and regulating station power. It is composed of two wireless access points (WAP), Server 1 (Panda) and Server 2 (Wave). Wave, located in Workman Room 342, is a desktop PC equipped with a 250GB external hard drive, used to archive the massive data. When this hard drive is filled up, the operator will manually replace it with another hard drive. As shown in Figure 3.1, Panda is put in a white shack at Pound Ranch, which is also the field site of the Server of LMA network and has the civil power line supply. It is used to collect system information and useful lightning data from some LEFA stations directly through the wireless network. Near the shack is a white box which houses the WILIGEAR CPU Board. Being attached to an omni-directional antenna, it works as a wireless access point (WAP) and connects the Pound Ranch sub-network of LEFA wireless network to a wired Langmuir network.

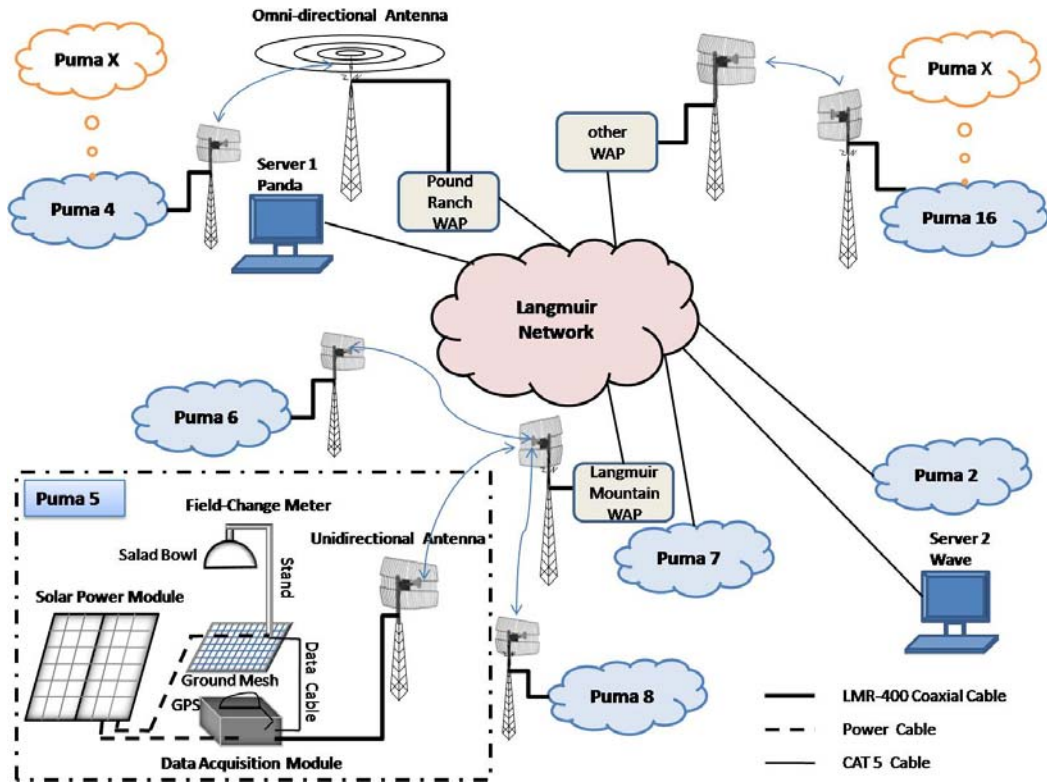


Figure 2.17 Current LEFA Network

As of October 2009, six stations have been deployed at different locations. As shown in Figure 2.17, Stations Puma2 and Puma7 are separately located on the roof of Workman Building and on the top of Langmuir Laboratory in the Magdalena Mountain. Both of them are directly connected into Langmuir network with ethernet cable. Station Puma4 is deployed at Pound Ranch. Through the Pound Ranch WAP, Station 4 is integrated into the Langmuir network. Stations Puma5, Puma6, and Puma8 are deployed on plains surrounding Langmuir Lab, communicating with Langmuir network through the Langmuir Mountain WAP. The omnidirectional antenna was placed at Pound Ranch for use in the calibration study. It was hoped that it would also provide a receiving point for many of the field stations. It was discovered during deployment that there were line of sight problems with the Pound Ranch site, so at present the omnidirectional antenna is only communicating with a single station.

CHAPTER 3 Initial Relative Gain Ratio Calibration

Three types of calibration on the LEFA were conducted in July, August and October of 2009. The self-calibration refers to obtain the gain ratios between different channels in each station. Cross-calibration is the gain ratios of sensitive channel between different collocated stations. Field calibration is a second cross-calibration done with instruments dispersed to their field positions and is the subject of Chapter 4. This chapter focuses on discussing self-calibration and first cross-calibration. It begins with the description of the calibration site and theoretical expectations for the calibration result. It concludes with a description of calibration procedure and discussion of results. Table 3.1 shows the complete definitions of variables used in this chapter and Chapter 4.

Variable	Description
S/M	self-gain ratio between S channel and M channel
M/I	self-gain ratio between M channel and I channel
Puma4/Puma6 Puma5/Puma6 Puma7/Puma6 Puma8/Puma6 Puma4/Puma5	cross-gain ratios between two different stations

Table 3.1 Definition of Variables that are referred to in the Calibration

3.1 Calibration Site and Theoretical Expectations

The initial calibration was conducted in July and August of 2009. In this calibration, four stations (i.e., Puma4, Puma5, Puma6 and Puma7) were deployed at the calibration site at Pound Ranch, shown in Figure 3.1. First-generation (see version A in Appendix B) analog boards were used on Station Puma4 and Station

Puma5. Second generation (version B in Appendix A) field-change boards were used in Station Puma6 and Station Puma7. In comparison with version B, version A does not contain trigger circuit and has slightly different values for the capacitor C1 in the charge amplifier. For version A boards, values of the parameters needed for calibration are listed in Table 3.2, and values for revision B are in Table 2.3. The basic configuration information, the board version and height of stand, is shown in Table 3.3.

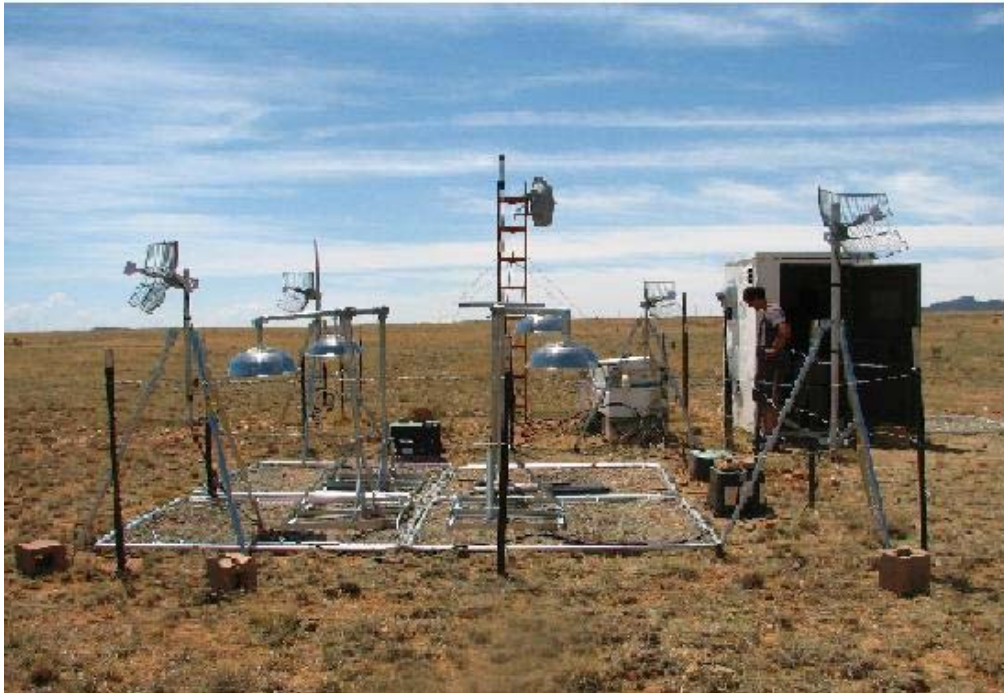


Figure 3.1 Calibration Site at Pound Ranch

Channel	Gain of Voltage Amplifier	Geometric Area (m ²)	C ₁ (nF)
Insensitive	-20	0.005	22
Medium	-20	0.02	5.2
Sensitive	-20	0.1	1.1

Table 3.2 Parameters of Version A of Analog Board

Station Name	Analog board	Height of stand (inch)
Puma4	Rev. A	50
Puma5	Rev. A	43
Puma6	Rev. B	43
Puma7	Rev. B	43.5

Table 3.3 Configuration of Calibration Stations

Four stations were deployed in a symmetric arrangement, shown in Figure 3.1. A fence was used to prevent the stations from being damaged by cattle. Pound Ranch was chosen because of the conveniences of local 120 VAC power and existing network connections. During the course of this calibration, several noise sources were discovered. These were fixed before the final field calibration.

Three factors which are known will affect the instrument sensitivity were known in advanced of the calibration study. These are effective areas of three sensor plates, the circuit design and shape factors. Shape factors include the length of arm of stand and height of stand. First the circuit design is considered only. Using Equation 2.10 and the parameters in Table 3.2, the theoretical self-gain ratios of three channels can be gotten by using their geometric areas as an estimate for the effective area. The results are shown in columns 2 and 5 of Table 3.4 under “Theoretical Ratio”. Cross calibration results can also be estimated using Table 2.3 and Equation 2.10. For example because gain G in the version B boards is halved, it is expected that the I-channel of Puma4 and Puma5 will be twice as sensitive as the I-channel on Puma6 and Puma7. The expected cross-calibration factors are shown in columns 2, 5 and 9 of Table 3.5.

Having tackled the easily understood problems, what remain are the more difficult to quantify factors. Puma4 has a different stand design than Puma5, 6, 7. This will probably change its cross-calibration. Also, the I-channel sensor plate is recessed beneath the M and S plates. This is handled by assigning an “effective

area” to the I-sensor, which is less than its geometrical area.

3.2 Calibration Procedure and Results

The least square error approximation method was selected to optimally calculate the relative gain ratios in each instrument (self-calibration) and cross-gain ratios between instruments (cross-calibration). Because of the noisiness and DC offset, it is necessary to preprocess the raw data. A digital low pass filter was used to clean the noisy data. The cut-off frequency of low pass filter was determined to be 25Hz by analyzing the noise. The last step of preprocess was to remove the DC offset. The M/I self-gain ratio of Puma6 and the data of 20090727-2350 were chosen to show the details of calibration procedure as below:

Step1: Extract a 2 second data segment. Select the data associated with a flash, which lasts 2 seconds, from the raw 1 min data shown in Figure 3.2.

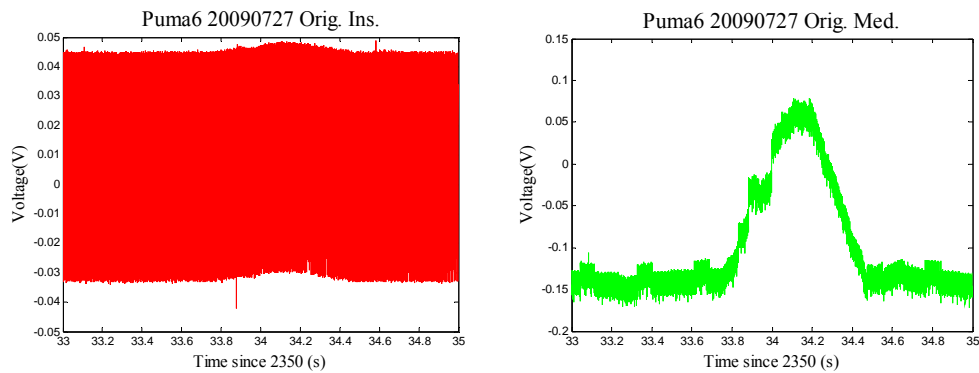


Figure 3.2 Original Flash from I channel and M channel of 20090727-2350

Step2: Analyze the noise from both raw data sets. By plotting data during interval from 33.001 to 33.01, it was observed the lowest frequency noise of I channel is around 300 Hz, shown as the envelope modulation in the left panel of Figure 3.3.

From the raw data of M channel shown in the right side of Figure 3.2, approximate 3.5 Hz noise is obvious as a square wave modulation. An examination of the M-channel of puma6 at higher resolution (right panel of Figure 3.3) shows that it also has a 300 Hz component and a structure that repeats roughly 50 times/second. In addition to these characteristic frequencies, all channels show a broadband white noise above 20 kHz.

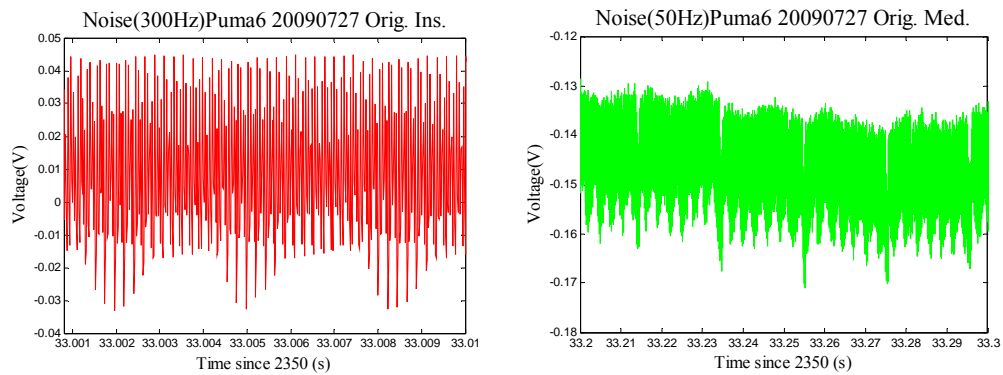


Figure 3.3 Noises from I channel and M channel of 20090727-2350

Step3: Clean raw data through low pass filter, shown in Figure 3.4 and extract the signals associated with lightning flash from the filtered data, shown in Figure 3.5. Digital low pass filter functions in Matlab: $[B,A] = \text{butter}(5,0.001)$; $\text{ych1} = \text{filter}(B,A,\text{ch1})$ are used to remove the high frequency noises. Parameter 5 in Butterworth function is the order of the filter. The cut-off frequency of filter is set to 25 Hz, corresponding to the parameter 0.001. The well-known end effect or boundary effect of filter is also shown in Figure 3.4. It is the positive step at 33 seconds in the left panel, and the negative step in the right panel. Since this is an artifact of the filter not present in the data, it was justified to truncate first 0.2 second of the data to remove the artifact.

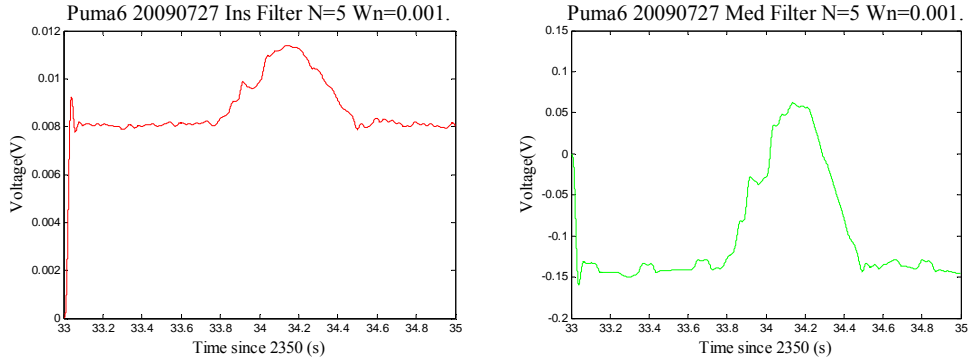


Figure 3.4 Flashes of Both Channels after Low Pass Filter

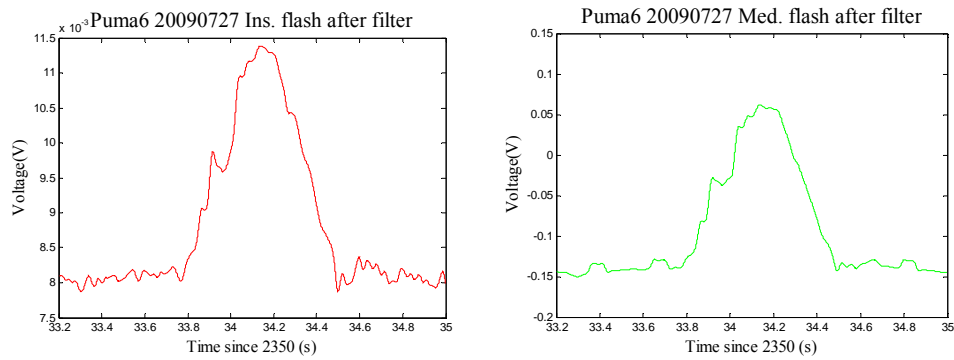


Figure 3.5 Flashes of Both Channels without Boundary Effect

Step4: Get the DC-offset of every channel by averaging one section, which should be zero theoretically and adjust the lightning flash after filter.

Step5: Apply the least square method to get the M/I self-gain ratio. Find the point where $\frac{\partial S}{\partial a} = 0$ and $\frac{\partial^2 S}{\partial a^2} > 0$, where $S = \sum_i (M_i - aI_i)^2$. The result is shown in Figure 3.6 and the M/I self-gain ratio of Puma6, a , is roughly 62, where S is minimum. The red line in right plot of Figure 3.6 stands for the product of I channel data and M/I self-gain ratio. The close agreement of the red and green curves assures that the selected value for a is reasonable.

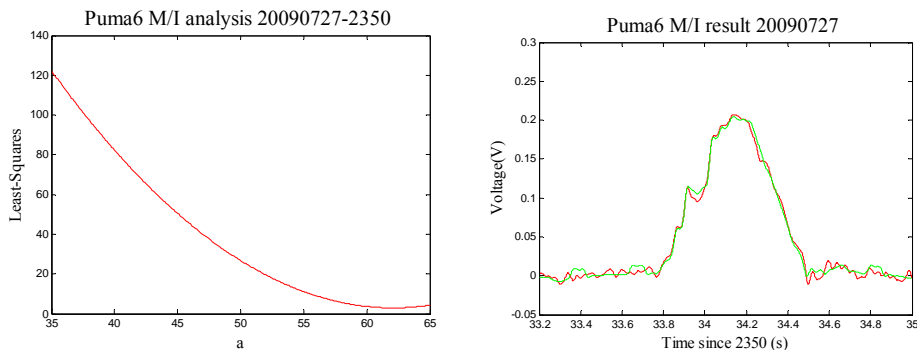


Figure 3.6 Result of Least Square Method

The filtering/fitting procedure just described was applied to data from three lightning flashes to obtain self-gain and cross-gain ratios for each of the four stations. The flashes selected were 20090727-2350 [33, 35], 20090727-2357 [45, 47], 20090728-2231 [54, 58]. The self-gain ratios obtained are shown in column 3, 6 of Table 3.4. Each value corresponds to the ratio obtained from a particular flash. Similarly, the cross-gain ratios for each flash are presented in columns 3, 6, and 10 of Table 3.5. Rows 1-3 in Table 3.5 show the measured cross-gain ratios. Row 4 shows the cross-gain ratio between Puma4 and Puma5 calculated using the data of first two rows in Table 3.5.

Station Name	Theoretical S/M ratio	Real S/M ratio	Real/Theo. of S/M ratio	Theoretical M/I ratio	Real M/I ratio	Real/Theo. of M/I Ratio
Puma4	25.45	22.4/23.2/23.1	0.88	15.714	40/39/38.3	2.49
Puma5	25.45	27.2/27.1/27.8	1.07	15.714	38/39/36	2.4
Puma6	25.83	29.1/29.9/28.7	1.13	28.387	62/63/64.4	2.22
Puma7	25.83	28.5/28.8/28	1.03	28.387	61/61/63.8	2.18

Table 3.4 Self-Calibration Result

Relative Ratio	Theo. S. Chan.	Real Sen. Chan.	Real/Theo. Sen. Chan.	Theo. M. Chan.	Real Med. Chan.	Real/Theo. Med. Chan.
Puma4/Puma6	1.091	1.52/1.466/1.532	1.38	1.19	1.975/1.79/1.86	1.576
Puma5/Puma6	1.091	0.967/0.972/0.963	0.887	1.19	1.035/0.97/0.98	0.995
Puma7/Puma6	1	1.203/1.198/1.179	1.193	1	1.225/1.21/1.2	1.212
Puma4/Puma5	1	1.572/1.51/1.591	1.56	1	1.91/1.84/1.9	1.833

Relative Ratio	Theo. I. Chan.	Real Ins. Chan.	Real/Theo. Ins. Chan.
Puma4/Puma6	2	3.03/2.92/3.05	1.5
Puma5/Puma6	2	1.68/1.65/1.76	0.85
Puma7/Puma6	1	1.26/1.24/1.23	1.24
Puma4/Puma5	1	1.804/1.77/1.733	1.77

Table 3.5 Cross-Calibration Result of Three Channels

3.3 Discussion of Results

There are a few hard to quantify factors which may affect the results of calibration, including the presence of a fence around the test area, radio antennas and other geometric factors. Reviewing Table 3.4 and 3.5, it is clear that most the measured values agree with predictions to within 25%. The only “strange” results involve Puma4 and the M/I ratio. Taking a close look at the real result, the following explanations for the abnormal calibration are proposed:

1. The experimental M/I ratios of all stations are more than twice their theoretical value

Since the sensor plate of I channel is 1.1 cm below the other plates, the effective area of the I-channel is much less than its geometric area. From the data, the

effective area of the I-channel is roughly 45% of geometric area. The theoretical edge effect calculation is made too. As shown in Figure 3.7, the geometric diameter of the I-channel sensor plate is 8 cm. Assumption is that the edge part of the I-channel sensor plate, with radial range equal to the vertical separation, is screened by the M-channel sensor plate. It is calculated that the effective I-channel sensor plate has a diameter of 5.8 cm, and thus the effective sensor area is about 53%, which is in remarkably good agreement with the 45% difference seen in the self-calibration study.

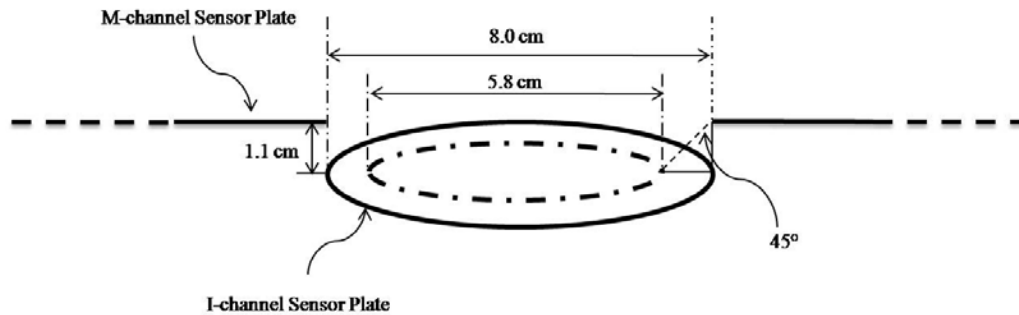


Figure 3.7 Edge Effect Calculation of I-Channel

2. Despite the fact that both Puma4 and Puma5 have Rev. A circuit boards, the last row of Table 3.5 shows that Puma4 is substantially more sensitive than Puma5 on all three of its channels.

It is because of the height of stand. The stand of Puma4 is 50 inches, while that of Puma5 is only 43 inches. As shown in Figure 3.8, the equipotential line near Puma4 is more intense than other stations, so the E-field Puma 4 measured is stronger than other stations measured.

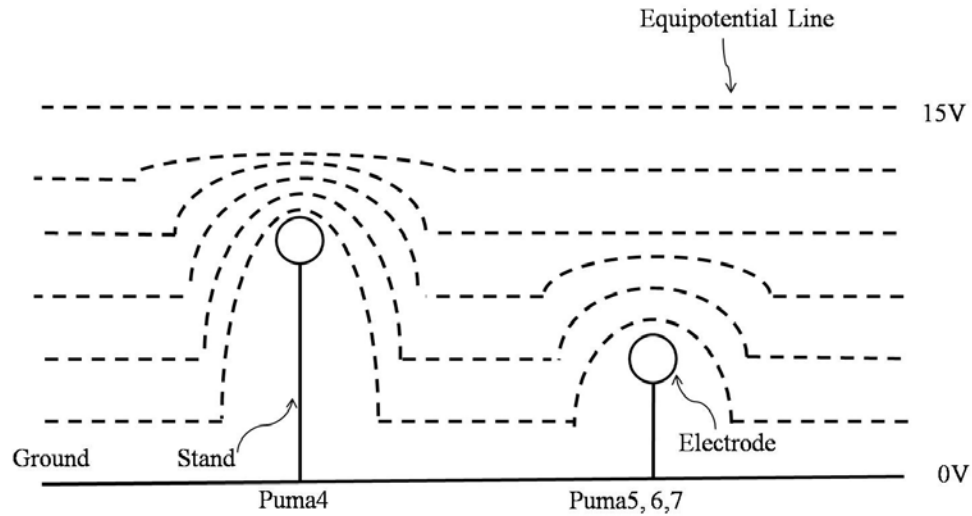


Figure 3.8 Impact of Height of Stand

3. The measured S/M ratio of Puma4 is noticeably lower than for Puma5, 6, 7. This is clear from examining either column 3 or column 4 of Table 3.4. By contrast, the theoretical values of S/M (shown in column 1) are almost identical for all stations.

The stand actually is grounded and it will decrease the density of Electrical field lines captured on the sensitive plate of salad bowl. Figure 3.9 shows that the E-field is reduced by the closeness of the grounded stand. Because the arm of Puma4 is shorter than others', Puma4's stand decreases the electrical field more than others in the sensitive plate. The length of the arm of stand doesn't affect the Medium channel as much as the S-channel. Therefore, the S/M ratio of puma4 is smaller than others. Also data from the last row of Table 3.5 validates the above guess, because the Real/Theoretical 1.56 of Puma4/Puma5 of S-channel is smaller than that value of M-channel 1.83.

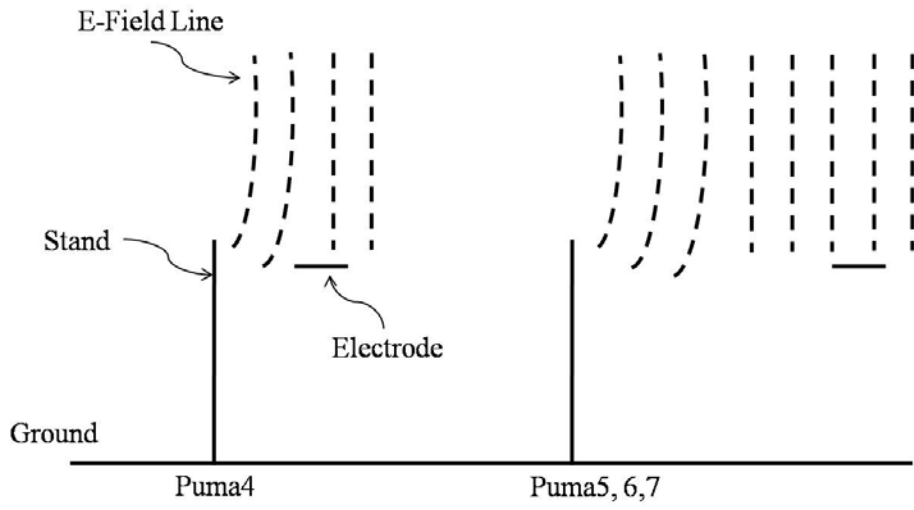


Figure 3.9 Impact of Arm of Stand

CHAPTER 4 Field Calibration and October 20, 2009 Storm

This chapter first describes the solutions to noise reduction, which had been done before the field calibration, and the basic theory of classic image problem for the analysis of calibration result. Then the procedure of field calibration is presented and the calibration result shows that the $1/r$ model is the best one to study the four chosen distant flashes. Result analysis of the second cross-calibration is considered. Finally, two typical examples of October 20, 2009 storm are chosen to show the basic knowledge of lightning type by initial data analysis, which shows current LEFA network running well.

4.1 Noise Reduction

The data analysis that went with the initial calibration helped to find most of noise sources. The following noise reduction steps were taken:

- 1) Replacing the Murata DC/DC converter with a different part made by Lambda. This eliminated the 300 Hz noise shown in Figure 3.3.
- 2) Fixing an obscure grounding problem in which the M-channel ground from the fast A/D converter board was also connected to the slow A/D board. This defeated the differential A/D and caused the 3.5 Hz noise shown in the right panel of Figure 3.2.
- 3) Shortening the data cables from 25 feet to 15 feet. This reduced high frequency noise.
- 4) Incorporating a low-pass filter board with $R = 100 \Omega$, $C = 0.015 \mu\text{F}$ into the DAM. Even a 15 foot data cable can pick up substantial noise before reaching the A/D. It is proper technique to put the filters as close to the A/D as possible.

These 4 steps reduced the total noise from 50 mV p-p to 2 mV p-p.

4.2 Classical Image Problem

Lightning is a giant electrical spark caused by the separation of electrical charge in a thunderstorm. The released electrical charge and the ground, which is looked as an infinite grounded conducting plate, constitute the classic image problem of Electrostatics. Suppose a point charge $+Q$ is held a distance d above an infinite grounded conducting plane, shown in Figure 4.1. Question: What is the potential in the region above the plane? It is easy to calculate the potential as:

$$V(x, y, z) = \frac{1}{4\pi\epsilon_0} \left[\frac{Q}{\sqrt{x^2 + y^2 + (z-d)^2}} + \frac{-Q}{\sqrt{x^2 + y^2 + (z+d)^2}} \right] \quad (4.1)$$

where x, y, z is the location of measurement point in three dimensional space, $\epsilon_0 = 8.854 \times 10^{-12}$ F/m is the permittivity of air. Then, the magnitude of E-field along the z axis in the region above the ground is gained:

$$E_z(x, y, z) = \frac{-\partial V(x, y, z)}{\partial z} = \frac{-1}{4\pi\epsilon_0} \left\{ \frac{-Q(z-d)}{[x^2 + y^2 + (z-d)^2]^{3/2}} + \frac{Q(z+d)}{[x^2 + y^2 + (z+d)^2]^{3/2}} \right\} \quad (4.2)$$

where z is the height of the sensor plate, and E_z is the measured lightning electric field. This simplifies when $z = 0$ to

$$E_z = \frac{1}{4\pi\epsilon_0} \frac{-2Qd}{(x^2 + y^2 + d^2)^{3/2}} \quad (4.3)$$

Notice $1/r^3$ dependence only works for electrostatic effect of lightning and negative E-field is for positive Q .

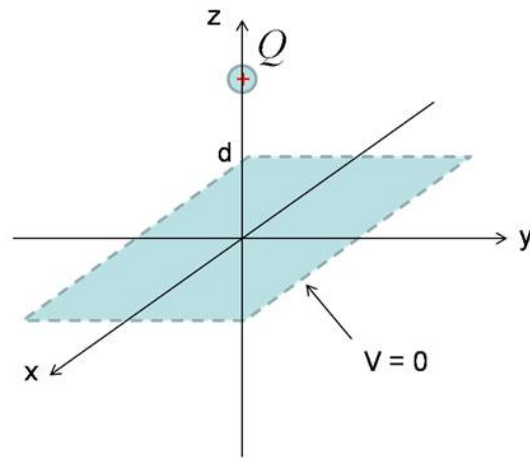


Figure 4.1 Classical Image Problem

However, according to the discussion of *Uman* [1987, pp.135-138] and *Bruce and Golde* [1941], it is realized that the induction effect, which depends on current I , and radiation effect, which depends on the change of current, dI/dt , of lightning discharges obey $1/r^2$ dependence and $1/r$ dependence, respectively. It was assumed that $1/r^3$ term would be appropriate for analysis. However, it is learned that $1/r^2$ or $1/r$ might be better, therefore, the analysis evaluated all three terms.

4.3 Cross-Calibration in the Field

After the successful initial calibration, in August and September of 2009 all stations were deployed to the field, including one more new station, Puma8. Table 4.1 lists the location of each station in terms of latitude, longitude, and altitude above mean sea level. In order to simplify the calibration, the analog boards of Puma4 and Puma5 were upgraded to the second generation design, version B, and the stand of Puma4 was also replaced by a new one of 43 inches high of the same design as the other stations deployed during the first stage of testing. In addition, all the noise reduction measures discussed in 4.1 were implemented. What should be mentioned

is that Puma2, as a test station located on the roof of Workman Center, still uses the old stand design, which is 50 inches high. The height 43 inches and 50 inches refers to distance between ground mesh and the bottom of the S-channel plate.

Station Name	Location	Longitude	Latitude	Altitude
Puma2	Workman Center Roof	106.907°W	34.066°N	1432m
Puma4	Pound Ranch	107.089°W	34.090°N	1843m
Puma5	Six-Mile	107.052°W	34.003°N	1916m
Puma6	k2-EMRTC	107.052°W	34.100°N	1816m
Puma7	Balloon Hangar	107.188°W	33.982°N	3226m
Puma8	d3-EMRTC	107.072°W	34.072°N	1851m

Table 4.1 Coordinates of Stations in the LEFA Network of October, 2009

In this calibration, the cross-gain ratio of the sensitive channel is considered. There are still several factors that may affect the accuracy in the electric field measurement at each LEFA station. These factors include the uncertainties in the local topography near the station and the mechanical design of each station. It is hard to quantify the impact of each individual factor, and therefore the relative gain is introduced to encompass all the unknown factors. Under the assumption that the altitudes of all stations are the same, the distance factor can be evaluated from the electrostatics Equation 4.2. The distance is measured as the range from the location where the charge is released by a lightning stroke to the measurement station. The experimental gain ratio between different stations can be determined using the least-squares method. Therefore, the following relationship is gained:

$$\text{Experimental Gain Ratio} = \text{Distance Factor Ratio} \times \text{Relative Gain Ratio}$$

Puma6 is chosen as the reference station primarily because this station is located in a relatively flat region with an open surrounding area, as shown in Figure 2.7. Once proper relative calibrations are obtained between the LEFA stations, if only one

station (e.g. Puma6) is calibrated vs. an absolute E-field standard, then the calibration can be propagated to all stations. Four distant lightning flashes are chosen to determine the experimental relative station gain ratio and they are referred to as Flash A, B, C, and E, respectively. The main reason that flashes at large distances are selected in the calibration is because of the attributes of lightning. A CG lightning flash comprises various discharge components, among which there are typically more than two high-current pulses called strokes that are initiated by downward-propagating leaders. For a distant flash, all stations only respond to the same return stroke. While for one at close range, it is possible that one station responds to the leader or preliminary breakdown process, while other stations may respond to the return stroke process. An example of the complexity of data from nearby flashes will be shown in Section 4.4. From the U.S. National Lightning Detection Network (NLDN), the time and locations of four CG flashes are listed in Table 4.2.

Flash	Time(on 10/20/2009)	Longitude	Latitude
A	19:16:27 UT	108.0483°W	34.9779°N
B	20:07:13 UT	107.7054°W	34.952°N
C	22:01:28 UT	106.5469°W	35.3923°N
E	22:54:48 UT	107.8155°W	34.1424°N

Table 4.2 Locations of Lightning Flashes used in Calibration

To find the relative gain ratios of the sensitive channel, the following calibration procedure was made:

Step 1: Calculate the distance factor ratios for each flash. First, the surface distance between the measurement station and the chosen lightning flash is calculated using the coordinates listed in Tables 4.1 and 4.2. Using Equation (4.2), the normalized lightning electric field can be obtained by assuming that Q is 1 C, the

altitude of measurement point is zero, and the height of point charge is 3 km above the ground level. In typical New Mexico thunderstorms, the altitude of the negative charge region is centered at 2-4 km above the ground level (at about 5-6 km MSL). The $1/r^2$ and $1/r$ model are also considered. The results are shown in Table 4.3 under the columns marked Ez . Then the normalized lightning electric field of each station is divided by that of Puma6 and the distance factor ratios are worked out for each flash, shown in column 3, 5, 7 of Table 4.4. Note that, whereas the estimates for Ez in the $1/r^3$ columns are reasonable, the magnitudes calculated for $1/r^2$ and $1/r$ are extremely large. This is because the electrical parameters for the inductive and radiation terms are not the same as those for the electrostatic terms. Since normalization of the field change will be made anyway and only trying to understand the relative distance dependence is interesting, do not worry that the fields listed in the $1/r^2$ and $1/r$ columns are completely unreasonable from a physical point of view.

Station Name	Flash A				Flash B			
	Surface Distance (km)	Ez of $1/r^3$ (mV/m)	Ez of $1/r^2$ (kV/m)	Ez of $1/r$ (MV/m)	Surface Distance (km)	Ez of $1/r^3$ (mV/m)	Ez of $1/r^2$ (kV/m)	Ez of $1/r$ (MV/m)
Puma2	145.6	17.42	2.544	370.49	122.7	29.181	3.582	439.64
Puma4	132.2	23.34	3.086	408.07	111.2	39.195	4.360	485.01
Puma5	141.7	18.95	2.686	380.69	121.3	30.202	3.665	444.7
Puma6	133.6	22.61	3.021	403.71	112.1	38.26	4.290	481.08
Puma7	135.9	21.48	2.920	396.92	117.8	32.973	3.886	457.92
Puma8	134.7	22.06	2.972	400.43	113.8	36.572	4.163	473.91

Table 4.3.1 Theoretical Estimation of Normalized E-field at Each Station

Station Name	Flash C				Flash E			
	Surface Distance (km)	E_z of $1/r^3$ (mV/m)	E_z of $1/r^2$ (kV/m)	E_z of $1/r$ (MV/m)	Surface Distance (km)	E_z of $1/r^3$ (mV/m)	E_z of $1/r^2$ (kV/m)	E_z of $1/r$ (MV/m)
Puma2	151.1	15.631	2.362	356.97	84.08	90.597	7.662	644.63
Puma4	153	15.056	2.304	352.58	67.13	177.817	11.95	803
Puma5	161.2	12.874	2.076	334.71	72.01	144.117	10.387	748.62
Puma6	150.9	15.693	2.369	357.48	70.44	153.952	10.854	765.25
Puma7	167.4	11.496	1.925	322.25	60.49	242.869	14.709	890.84
Puma8	154.5	14.622	2.260	349.24	68.9	160.487	11.34	782.07

Table 4.3.2 Theoretical Estimation of Normalized E-field at Each Station

Step 2: Determine the experimental gain ratio by fitting the lightning electric fields measured by Puma6 and other stations. Similar to the initial calibration, Flash A is taken for example and the measurements at Puma6 and Puma8 are plotted in Figure 4.2. Figure 4.3 shows the details about the spikes shown in both panels of Figure 4.2, demonstrating the different DC offsets in two measurements. After subtracting the DC offsets and trivial time offset from both measurements in comparison, the least squares method was used to get the experimental gain ratios. The least squares method means fitting data using many discrete data points over time since data of all stations has the exact UT time from the GPS. For the same lightning flash far away about 100 km, the measurements of two stations have a trivial time offset of the order of tens of microseconds. Figure 4.4 shows the fitting result. All experimental gain ratios for four flashes are shown in Table 4.4. Notice as the result of the hardware noises fixed, the data are very clear and it is not necessary to filter it, as what was done in the initial calibration.

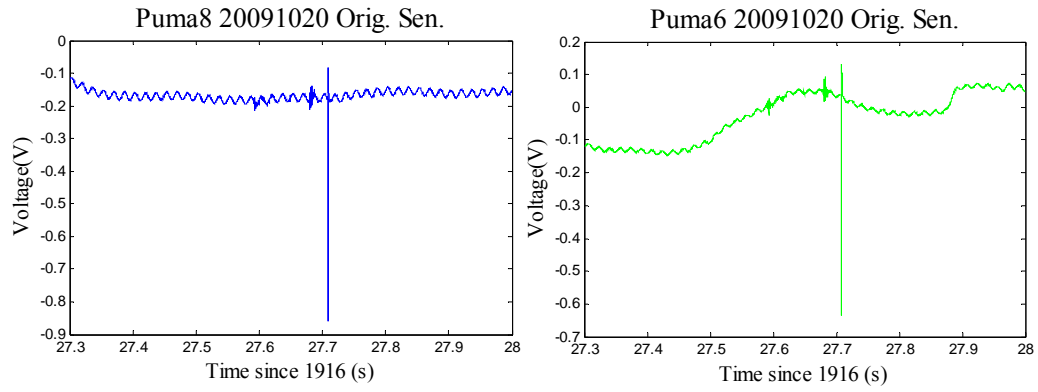


Figure 4.2 Distant Flashes of Puma6 and Puma8

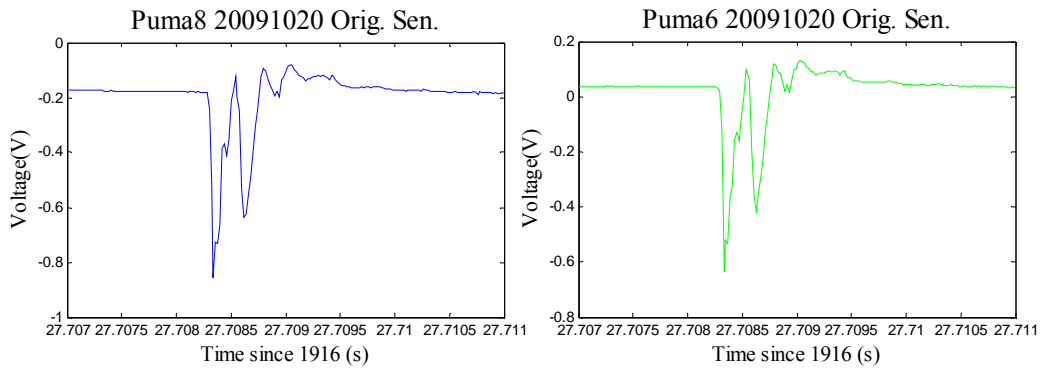


Figure 4.3 Distant Flashes by Zooming In

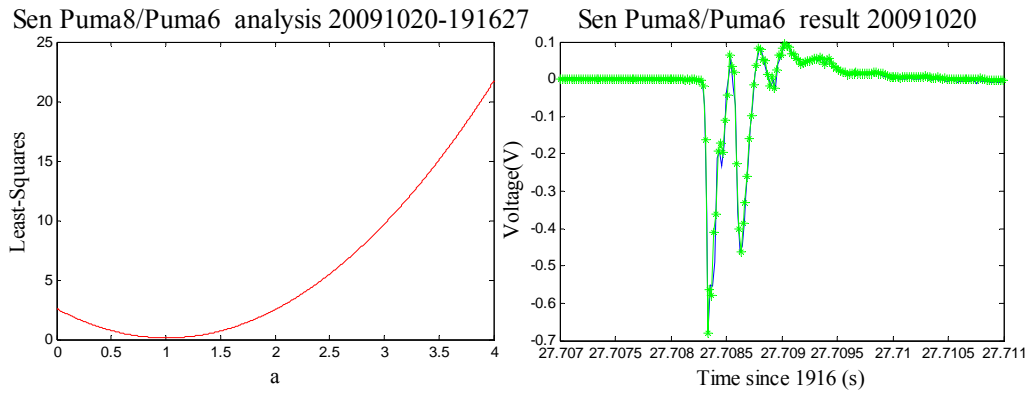


Figure 4.4 Fitting Result

Step 3: Calculate the relative-gain ratio using the known relationship regarding the distance factor ratio and experimental ratio. The final results for all the LEFA stations in deployment are plotted in Table 4.4.

Flash A	Experimental Ratio	Distance Factor Ratio of $1/r^3$	Relative Gain Ratio of $1/r^3$	Distance Factor Ratio of $1/r^2$	Relative Gain Ratio of $1/r^2$	Distance Factor Ratio of $1/r$	Relative Gain Ratio of $1/r$
Puma2/Puma6	1.243	0.77	1.614	0.842	1.476	0.917	1.355
Puma4/Puma6	0.741	1.032	0.718	1.022	0.725	1.011	0.733
Puma5/Puma6	0.662	0.838	0.79	0.889	0.745	0.943	0.702
Puma7/Puma6	2.115	0.95	2.226	0.967	2.187	0.983	2.151
Puma8/puma6	1.013	0.976	1.038	0.984	1.029	0.992	1.021

Table 4.4.1 Real Calibration Result for Flash A

Flash B	Experimental Ratio	Distance Factor Ratio of $1/r^3$	Relative Gain Ratio of $1/r^3$	Distance Factor Ratio of $1/r^2$	Relative Gain Ratio of $1/r^2$	Distance Factor Ratio of $1/r$	Relative Gain Ratio of $1/r$
Puma2/Puma6	1.19	0.763	1.56	0.835	1.425	0.914	1.302
Puma4/Puma6	0.722	1.024	0.705	1.016	0.711	1.008	0.716
Puma5/Puma6	0.678	0.789	0.859	0.854	0.794	0.924	0.734
Puma7/Puma6	1.987	0.862	2.305	0.906	2.193	0.952	2.088
Puma8/puma6	1.039	0.956	1.087	0.970	1.071	0.985	1.055

Table 4.4.2 Real Calibration Result for Flash B

Flash C	Experimental Ratio	Distance Factor Ratio of $1/r^3$	Relative Gain Ratio of $1/r^3$	Distance Factor Ratio of $1/r^2$	Relative Gain Ratio of $1/r^2$	Distance Factor Ratio of $1/r$	Relative Gain Ratio of $1/r$
Puma2/Puma6	1.35	0.996	1.355	0.997	1.354	0.998	1.353
Puma4/Puma6	0.58	0.959	0.605	0.973	0.596	0.986	0.588
Puma5/Puma6	0.665	0.82	0.811	0.876	0.759	0.936	0.71
Puma7/Puma6	1.998	0.733	2.727	0.813	2.458	0.901	2.216
Puma8/puma6	1.041	0.932	1.117	0.954	1.091	0.977	1.066

Table 4.4.3 Real Calibration Result for Flash C

Flash E	Experimental Ratio	Distance Factor Ratio of $1/r^3$	Relative Gain Ratio of $1/r^3$	Distance Factor Ratio of $1/r^2$	Relative Gain Ratio of $1/r^2$	Distance Factor Ratio of $1/r$	Relative Gain Ratio of $1/r$
Puma2/Puma6	1.357	0.588	2.306	0.706	1.922	0.842	1.611
Puma4/Puma6	0.912	1.155	0.79	1.101	0.828	1.049	0.869
Puma5/Puma6	0.714	0.936	0.763	0.957	0.746	0.978	0.730
Puma7/Puma6	2.009	1.578	1.273	1.355	1.483	1.164	1.726
Puma8/puma6	1.004	1.042	0.963	1.045	0.961	1.022	0.983

Table 4.4.4 Real Calibration Result for Flash E

Flash A,B,C	Relative Deviation of $1/r^3$	Relative Deviation of $1/r^2$	Relative Deviation of $1/r$
Puma2/Puma6	0.0925	0.0428	0.0225
Puma4/Puma6	0.0924	0.1045	0.1167
Puma5/Puma6	0.0438	0.0329	0.0233
Puma7/Puma6	0.1108	0.0679	0.0297
Puma8/puma6	0.0369	0.0297	0.0224

Table 4.5 Relative Deviation of Relative Gain Ratio for Flashes A, B, and C

Comparing the results listed in Table 4.5, the $1/r$ model has the smallest relative deviation, which means this model might be most appropriate to describe the variation of lightning electric field over distance when the distance is greater than 100 km. Furthermore, the wave-shapes in Figure 4.3 make more sense interpreted as proportional to the return stroke current (which has a very sharp rise) or the return stroke current derivative (which would be expected to have multiple peaks) rather than as proportional to the charge transferred, which should look more like a step. (As in Figure 4.10, bottom panel). Thus in what follows a distance dependence of $1/r$ will be adopted to discuss calibration factors. The results of this calibration confirm and further demonstrate the benefits of using distant flashes for the determination of relative-gain ratios in multi-station electric field measurements. The main results of this work are summarized as follows:

1. Ratios of Puma4/Puma6 are close to each other for Flashes A, B, and C, ranging between 0.588 and 0.733, which indicates that Puma4 is a little less sensitive than Puma6 because of they are located at different geographic locations. Similarly, ratios of Puma5/Puma6 vary from 0.702 to 0.734 for the four flashes. Ratios of Puma8/Puma6 are between 0.983 and 1.066 for four measurements, indicating that that Puma8 almost has the same sensitivity with Puma6. Puma8/Puma6 ratio is reasonable and close to what expected. While Puma4/Puma6 and Puma5/Puma6 is lower than 1, and currently the reason still is unknown.

2. Ratios of Puma2/Puma6 are roughly 1.302-1.355 for Flashes A, B, and C. This indicates that Puma2 is more sensitive than Puma6. As mentioned above, Puma2 is located on the roof of Workman Center, and thus the ambient electric field around Puma2 is thus significantly distorted, shown in Figure 4.5.

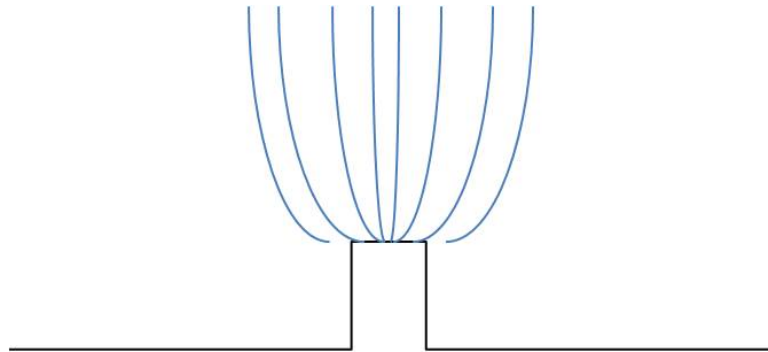


Figure 4.5 E-field Distortion around Elevated Objects

3. Ratios of Puma7/Puma6 are between 2.088 and 2.216 for Flashes A, B, and C. This also indicates that Puma7 is the most sensitive of all instruments. Obviously, it is because Puma7 is located on a mountain ridge at Langmuir Laboratory. Approximating a mountain ridge as a cylinder, one can readily understand the field enhancement of roughly a factor of 2 that Puma7 demonstrates compared to the instruments on flat land.

4. For Flash E, Puma2/Puma6 is 1.611, which is larger than the results for other three flashes. For Flash E, Puma7/Puma6 is only 1.27, much smaller than other three flashes. Taking a close look at the data in Table 4.4, their distance factor ratios had a big difference. Then back to Table 3.4, the distance of Puma2 is 84 km, and the distance of Puma7 is about 60 km. Using Equation (4.2) with $d = 3$ km, $z = 0$ and $r = \sqrt{x^2 + y^2 + d^2}$, where x, y, z is the location of measurement station in three dimensional space. The normalized lightning electric field as a function of the surface distance $R = \sqrt{x^2 + y^2}$ is plot in Figure 4.6. For Flashes A, B, C, such assumption is made that the flash maybe treated as a single point. Flash E is closer. It is 60 km from the nearest station and 85 km from the farthest station. As shown in Figure 4.4, between 60 and 85 km normalized field changes from 250 mV/m to 80 mV/m (about a factor of 3). Because of its proximity, Flash E is very sensitive to distance. If the model of a flash as a point is approximate, the approximation is perhaps invalid for Flash E. Thus nearby flashes are more sensitive to the distance factor. For Flash E, the point flash model may not work.

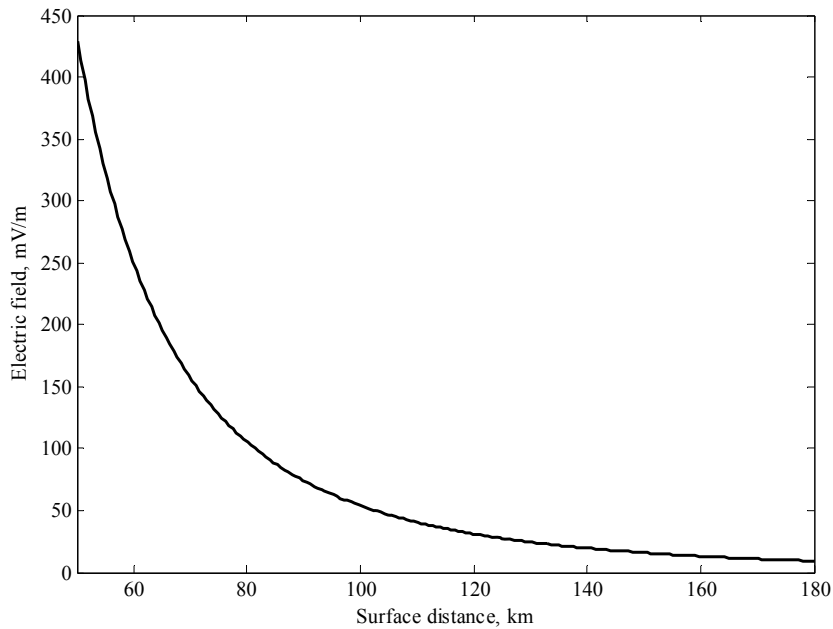


Figure 4.6 The Surface E-field as a Function of Surface Distance

4.4 Initial Data Analysis

In the following, two examples of NCG and IC, separately, will be taken to demonstrate basic details of them.

4.4.1 Example of a Multi-Stroke Negative Cloud-to-Ground Flash

Figure 4.7 shows the drawing illustrating two main processes comprising a negative cloud-to-ground flash. NCG flash is initiated by a downward-moving negatively charged leader, as shown, and hence lowers negative charge to ground. In the idealized model of the cloud charges also shown in Figure 4.7, the main charge regions, P and N, are of the order of many tens of coulombs of positive and negative charge, respectively, and the lower p region contains a smaller positive charge. There are two types of leader. They are stepped leader, which initiates the first return stroke in a flash by propagating from cloud to ground in a series of discrete steps, and dart leader, which occurs just before a secondary lightning strike. The dart leader is distinguished from the stepped leader by having fast process. A dart leader may transform to a step leader (or vice versa) depending on the state of the ionization of the path [Uman, 1987]. The stepped leader is itself initiated by a preliminary breakdown within the cloud. The breakdown is shown in the lower part of the cloud between the N and P regions in Figure 4.7. When the negative leader descends toward ground, the E-field change on the ground is positive. Once the leader tip is connected to ground potential, the visible discharge of electricity between storm cloud and an earthing point at ground level happens, and it is also called a return stroke [Uman]. The return stroke effectively lowers to ground the charge originally deposited on the stepped leader channel as well as other charges that may be available to the top of its channel. It leads to a negative change of lightning E-field.

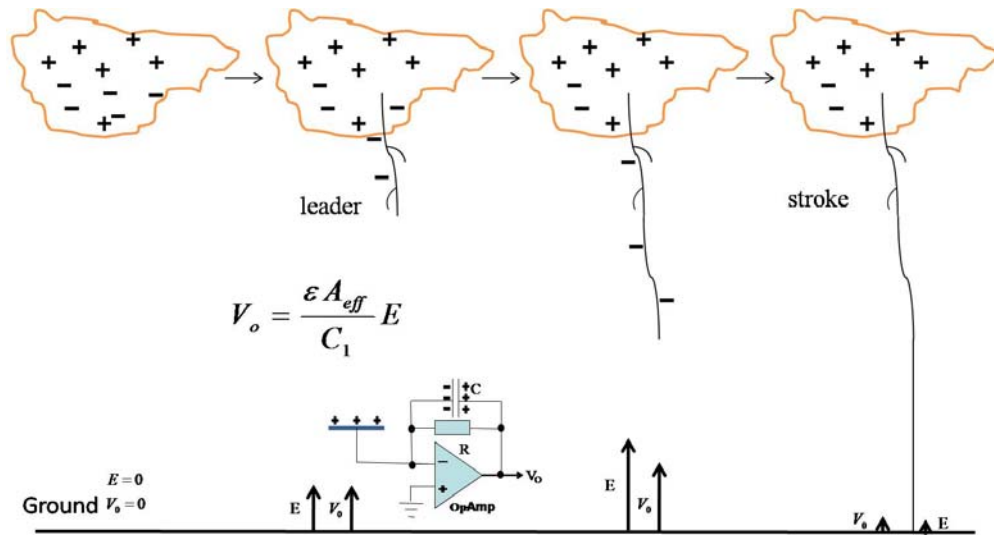


Figure 4.7 Drawing of Two Main Processes in NCG

Figure 4.7 also shows how the slow antenna responds to the change of E-field due to NCG lightning flash. When the negative charge descends toward ground, a positive charge is induced on the surface of the sensor plate, meanwhile, a negative charge is induced on the electrode side of the capacitor. This induces an opposite charge on the other side of the capacitor. Thus, the output of charge amplifier is positive voltage during the leader process of NCG flash. It has same direction as E-field. Also because this charge amplifier is followed by an inverting operational amplifier, the corresponding output of analog board is negative. The Puma2 panel of Figure 4.8 illustrates the leader and return stroke process just discussed. Between 49.75 and 49.78 second, and again 49.83 and 49.85 second, negative going voltages corresponds to a positive going E-field from an approaching negative leader. At 49.78 and 49.85 second, a positive step change in voltage corresponds to a return stroke.

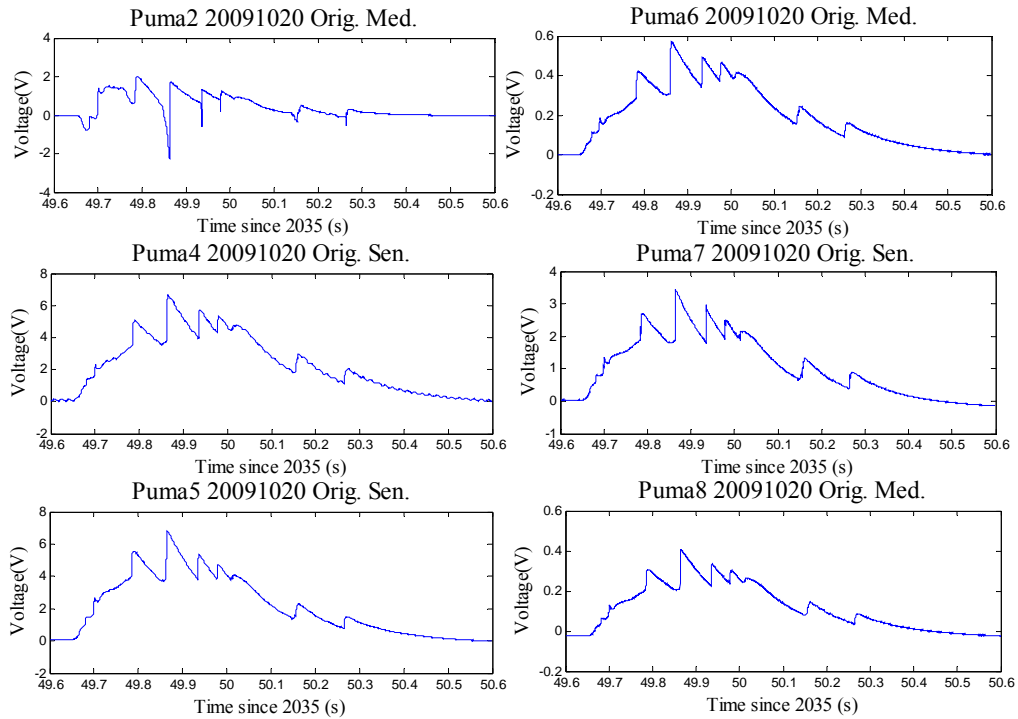


Figure 4.8 Original Plots of Six Stations

Figure 4.8 shows the measurement of a multi-stroke negative cloud-to-ground lightning flash. Five return strokes were located by the NLDN. The NLDN data for this NCG flash is in Table 4.6. The distances between each stroke and the measurement stations were calculated and shown in Table 4.7. From Table 4.7, Puma2, Puma6 and Puma8 are the three closest stations to this flash, which is also shown in Figure 4.11, and the sensitive channels are saturated. This is why the original data of medium channels for these stations were plot in Figure 4.8. This flash gives an example of the advantage of three-channel design for field-change meter. Notice Figure 4.8 also shows that the wave of Puma2 is different from waves of other stations for the same flash. This is because Station Puma2 is at the closest distance, shown in Table 4.6 and Figure 4.10. Because it is closest, leader creates positive ΔE as described before. For other stations is ΔE negative described in next section.

UT Time	Latitude	Longitude	Peak Current	Return Stroke #
20:35:49.784	34.0899	-106.9362	-10.0 kA	3
20:35:49.863	34.0770	-106.9092	-20.0 kA	4
20:35:49.935	34.0762	-106.9100	-30.0 kA	5
20:35:49.977	34.0763	-106.9091	-15.0 kA	6
20:35:50.264	34.0766	-106.9081	-13.0 kA	9

Table 4.6 NLDN Recordings for the Negative CG Lightning Flash

Station Name	Distance Range (km)
Puma2	1.1 to 3.1
Puma4	14 to 17
Puma5	15 to 16
Puma6	9 to 14
Puma7	26 to 28
Puma8	12 to 16

Table 4.7 Distance Range between this NCG Flash and Stations

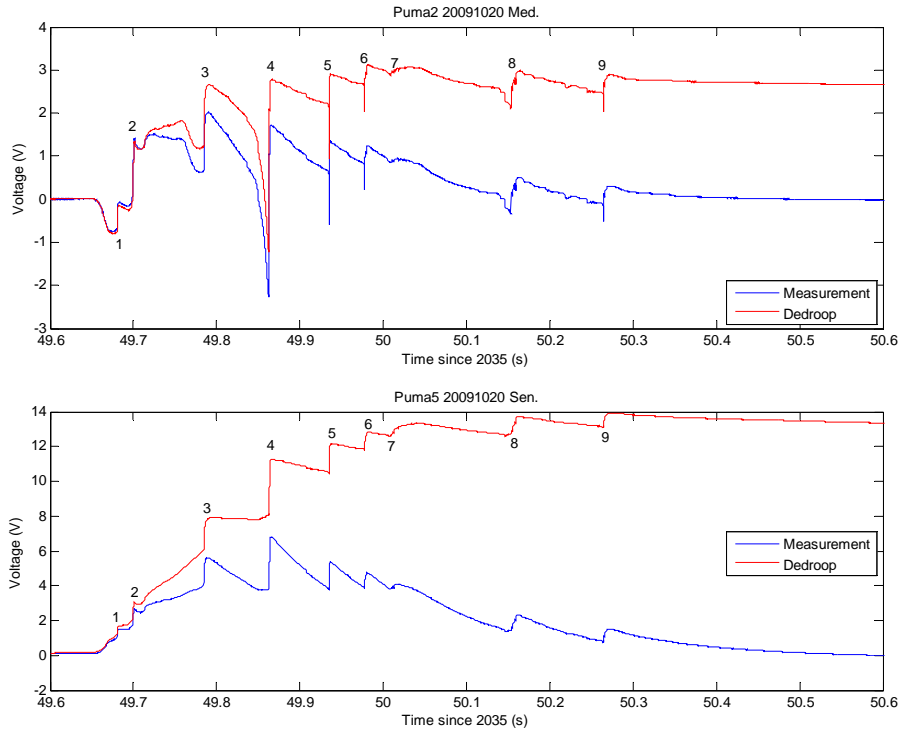


Figure 4.9 Original Plots vs. Dedrooped of Puma2 and Puma5 (Voltage Signal)

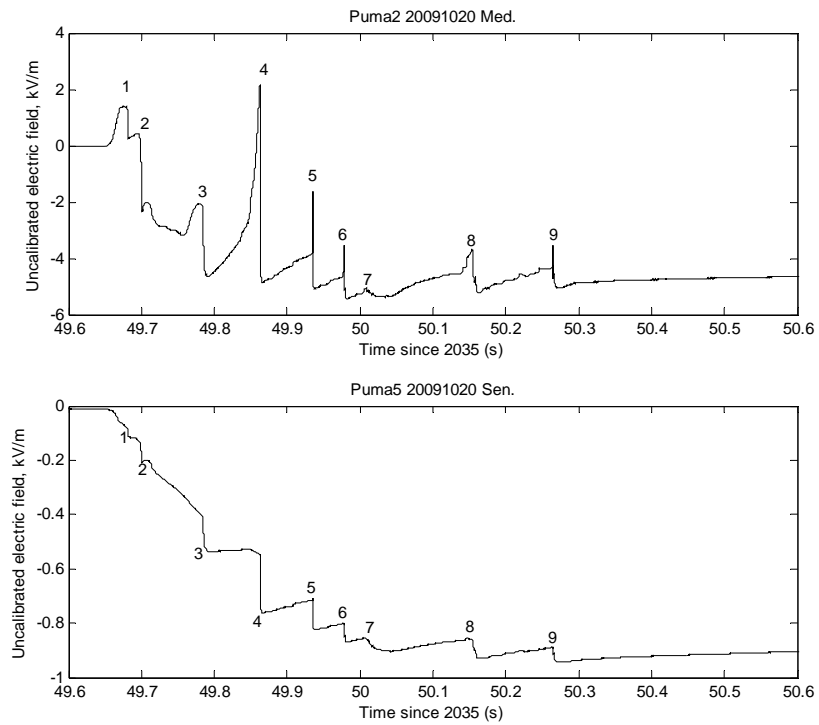


Figure 4.10 Uncalibrated E-field of Puma2 and Puma5 after Dedrooping

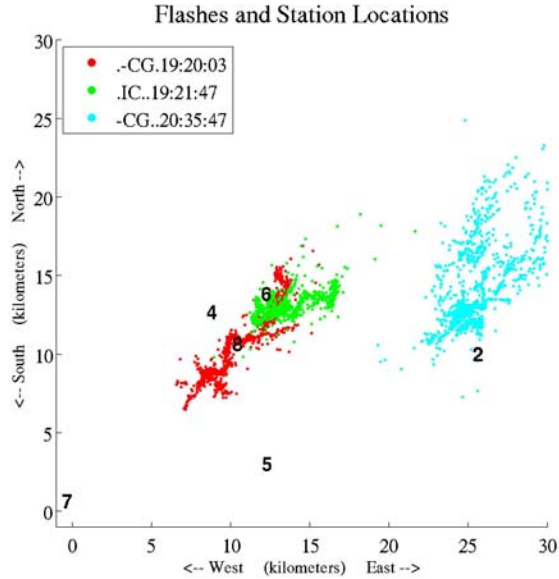


Figure 4.11 Flashes and Station Locations

Figure 4.9 shows the results of dedrooping process for one close station Puma2 and one distant station Puma5. In the top panel of Figure 4.10, Strokes 1, 3, and 4 clearly show the 20 ms rise in the E-field from a negative stepped leader. A fully developed stepped leader lowers up to 10 or more coulombs of negative cloud charge toward ground in tens of milliseconds. The leaders of Strokes 5, 6, and 9 are fast processes, and they are dart leaders. The location error of the NLDN is known to be 100 m or greater [Idone *et al.*, 1998]. Given this error, Table 4.6 shows Strokes 4, 5, 6, and 9 came to ground at the same point. Stroke 3 came to ground about 3 km from other strokes. It thus fits that Strokes 3 and 4 exhibit stepped leaders. Strokes 5, 6, and 9 are dart leaders because they use the channel already ionized by Stroke 4.

Notice that the leader of Stroke 1 in Puma2 is positive change, while Puma5 shows that it is negative change of E-field. To understand this, the concept of reversal distance is needed and shown in Figure 4.11. The E-field on the ground is

$$E = \frac{Q}{4\pi\epsilon_0} \left[\frac{h}{(r^2 + h^2)^{3/2}} - \frac{H}{(r^2 + H^2)^{3/2}} \right] \quad (4.4)$$

where r is the horizontal distance between the lightning flash and the measurement station, h is the height of negative leader above the ground level, and H is the height of positive thunderstorm cloud above the ground level. When $r = 0$, $E > 0$; $r \gg H$, $E < 0$. If assuming $h = 3$ km, $H = 10$ km, the reversal distance is roughly 8 km. It means if the measurement station is far away more than 8 km, the E-field changes due to the leader from positive to negative.

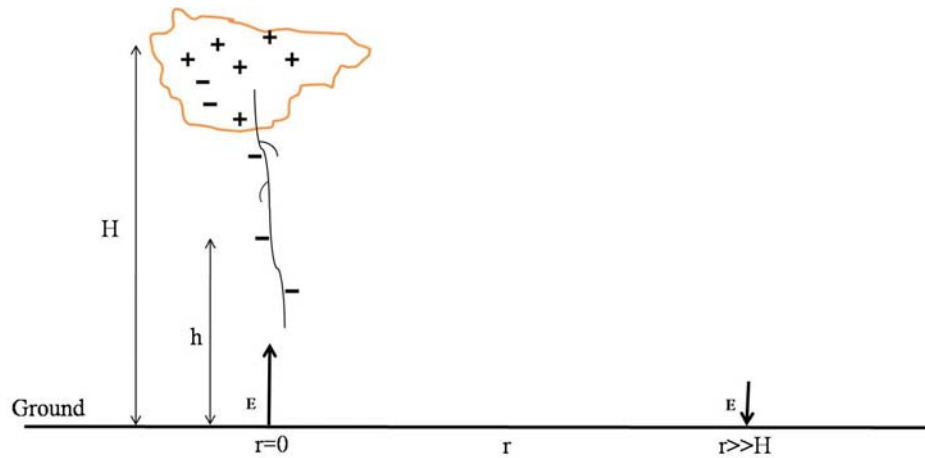


Figure 4.12 Concept of Reversal Distance

4.4.2 Example of an Intracloud Flash

Figure 4.13 shows the temporal development of an experimentally measured IC flash, in cartoon form. The typical New Mexico isolated thunderstorm cloud extends over about 10 km, and the cloud top is usually at ~ 10 km altitude above the ground level. The breakdown began between the two charge levels and progressed upward with time, then outward along the upper level channels, which is a positive charge region of the cloud. Significant radiation was not detected in the lower level, negative charge region until after a time delay of tens of milliseconds. After the lightning flash, the net charge structure shows in the last thunderstorm cloud of Figure 4.13. This sequence of events is typical of IC flashes observed at VHF [Rison *et al.*, 1999]. The two electric field vectors shown in Figure 4.13 represent the different

field changes which would be seen by instruments located under different parts of the cloud. The instrument on the left sees effect of removal of negative charge overhead, while the instrument at right sees destruction of positive charge.

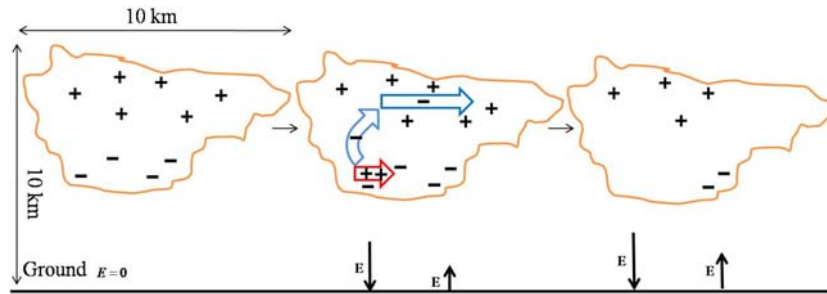


Figure 4.13 Drawing of IC flash

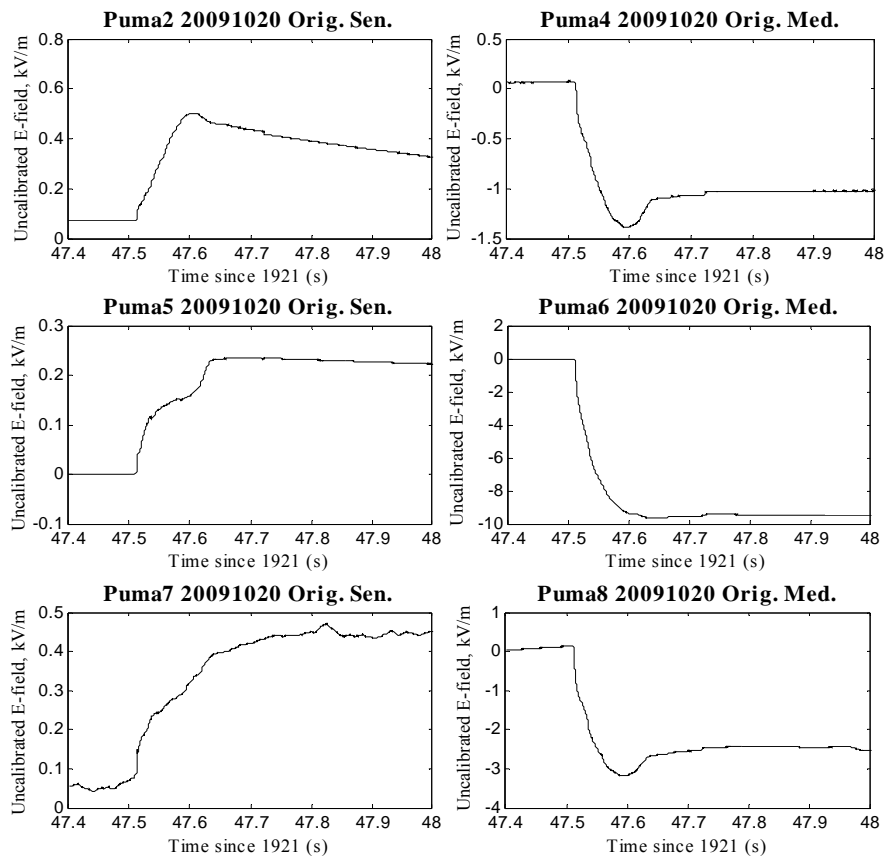


Figure 4.14 Uncalibrated E-field of Six Stations after Dedroo

Figure 4.14 shows an example of IC flash, which occurred at 19:21:47 UT, on 20 October, 2009. Puma2, 5, 7 got the positive E-field because they were far away from the flash. While other three stations are close to the flash, also shown in Figure 4.11 and got the negative E-field. Figure 4.15 shows the result of dedrooping process for station Puma4, a close station, and station Puma5, a distant station.

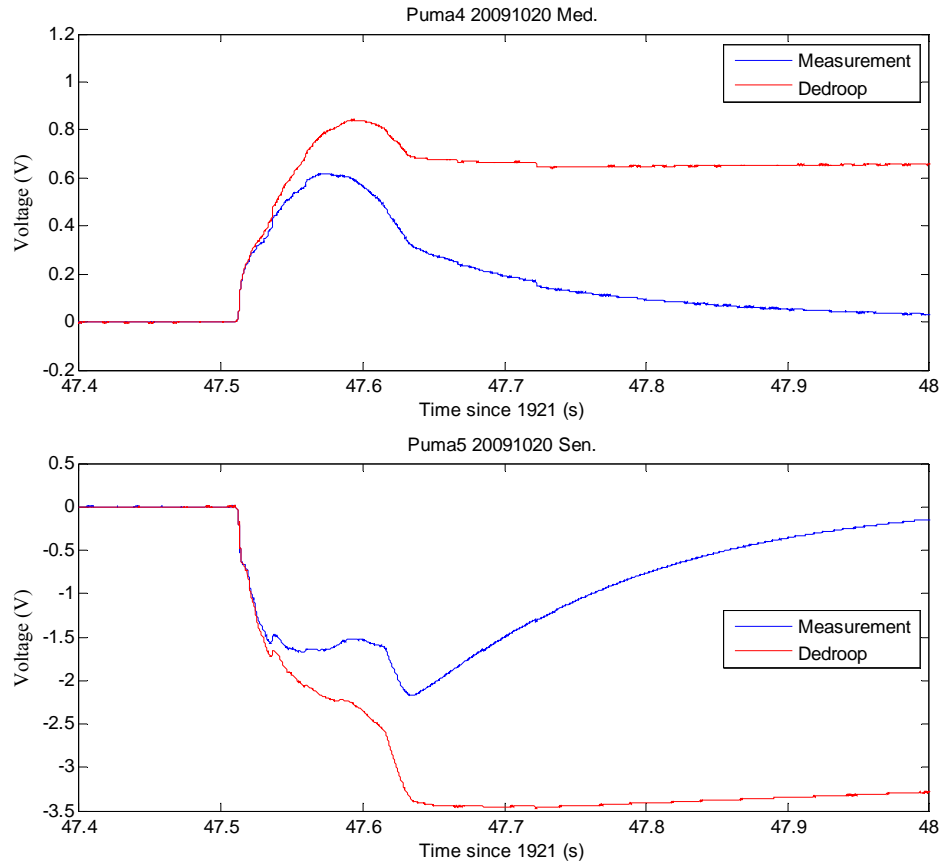


Figure 4.15 Original Plots vs. Dedrooped of Puma4 and Puma5 (Voltage Signal)

Considering now the data presented in section 4.4, it is realized that IC and CG flashes differ in two ways when measured at multiple locations. First, the CG flash usually has an identifiable sharp return stroke feature, while the IC does not. Second, the CG return stroke has the same polarity at all stations, but the overall field change from an IC flash may well have a different sign for the nearby and the more distant stations.

CHAPTER 5 Summary

This thesis presents the following content: description of system hardware integration, analysis and characterization of sensors and electronics of the field-change meter, calibration and initial data analysis. In the LEFA system, data acquisition module (DAM) parts are integrated in a rugged aluminum box, and water-proof connectors are applied for outdoor operation. GPS signals are fed into the DAM to get the exact timing, which is essential for the inter-station correlation and the comparison with LMA observations and NLDN recordings. Temperature sensors are also installed into the DAM to acquire the system status. As the solar power module and wireless module are integrated, the station can operate for an entire thunderstorm season in New Mexico at a remote field location. The field-change meter has three channels, named “sensitive,” “medium,” and “insensitive”, each with different sensor plates and gains to detect the E-field over a different range from 21 mV/m to 496 kV/m. Circuit analysis of each channel shows the corresponding theoretical maximum values of the E-field that could be measured on each channel are 0.678 kV/m, 17.506 kV/m, 496 kV/m, respectively, and the dedrooping procedure is used to retrieve the true E-field value from the resulting voltage.

From a whole project view, a coordinated network of field-change instruments has been built and it satisfies all design requirements. It can measure the electrostatic effects and some inductive effects owing to the sustained 50 kS/second data sampling rate of the DAM, and has a large dynamic measurement range because of its three-channel design of the FC meter and multi-station deployment. It can operate for the entire thunderstorm season in the field because of the integration of solar power and wireless communication system and has inter-station correlation and correlation with LMA and NDLN due to the exact GPS time.

The initial calibration and field calibration was conducted using the data acquired during two New Mexico thunderstorms in July and October, 2009. The least-squares method is applied to estimate the self-gain and cross-gain ratios in the calibration procedure. Two forms of calibration were performed during the initial calibration: self-calibration and cross-calibration. Self-calibration was conducted to determine the experimental gain ratios between the three channels on one station by recording the same lightning strikes and taking the ratio of signal strengths. Results of self-calibration show that:

(1) the experimental S/M ratios of Puma5, Puma6, Puma7 are greater than the theoretical values, which were calculated using the geometrical areas of sensors, by approximately 13%. This is because their effective areas of sensitive channel are greater than their physical areas.

(2) the experimental S/M ratios of Puma4 is less than its theoretical one by 12%. Since its shorter arm of stand greatly decreases the electrical field around the S-channel.

(3) the real M/I ratios of all stations are more than twice those predicted. The reason is that the effective area of insensitive channel is much less than the geometric area because of its mechanical design. Experimental data analysis shows that the effective area of the I-channel is roughly 45% of the geometric area.

Cross-calibration was conducted by symmetrically placing 4 stations at the same site and taking the ratios of recorded signals from the same lightning strikes for three channels across stations. Results show that (1) Puma4 is much more sensitive than Puma6 through all channels by about 50%, (2) Puma5 is little less sensitive than Puma6 by roughly 15%, and (3) Puma7 is more sensitive than Puma6 by approximately 24%. These differences are determined to be due to the different height of stand at each station. Since the shape of ground in field location impacts greatly the result of cross-calibration and the different stand also plays a key role in the self-calibration, the results of initial calibration will not be used in the future.

The field calibration includes the distance dependence calibration and second cross-calibration. All stations were unified using same stands and same version of analog boards and deployed at their individual field locations. The field calibration was performed by taking the experimental ratio of recorded signals from the same distant lightning flash and then dividing the distance factor with different distance dependence models ($1/r$, $1/r^2$ or $1/r^3$), to get gain ratios of sensitive channel across stations. The distance dependence calibration is most self-consistent when the distance dependence of the flash is modeled as $1/r$, though gross features of instrument sensitivity persist regardless of whether the distance dependence is $1/r$, $1/r^2$ or $1/r^3$. This dependence suggests that for flashes >100 km away the radiation field dominates.

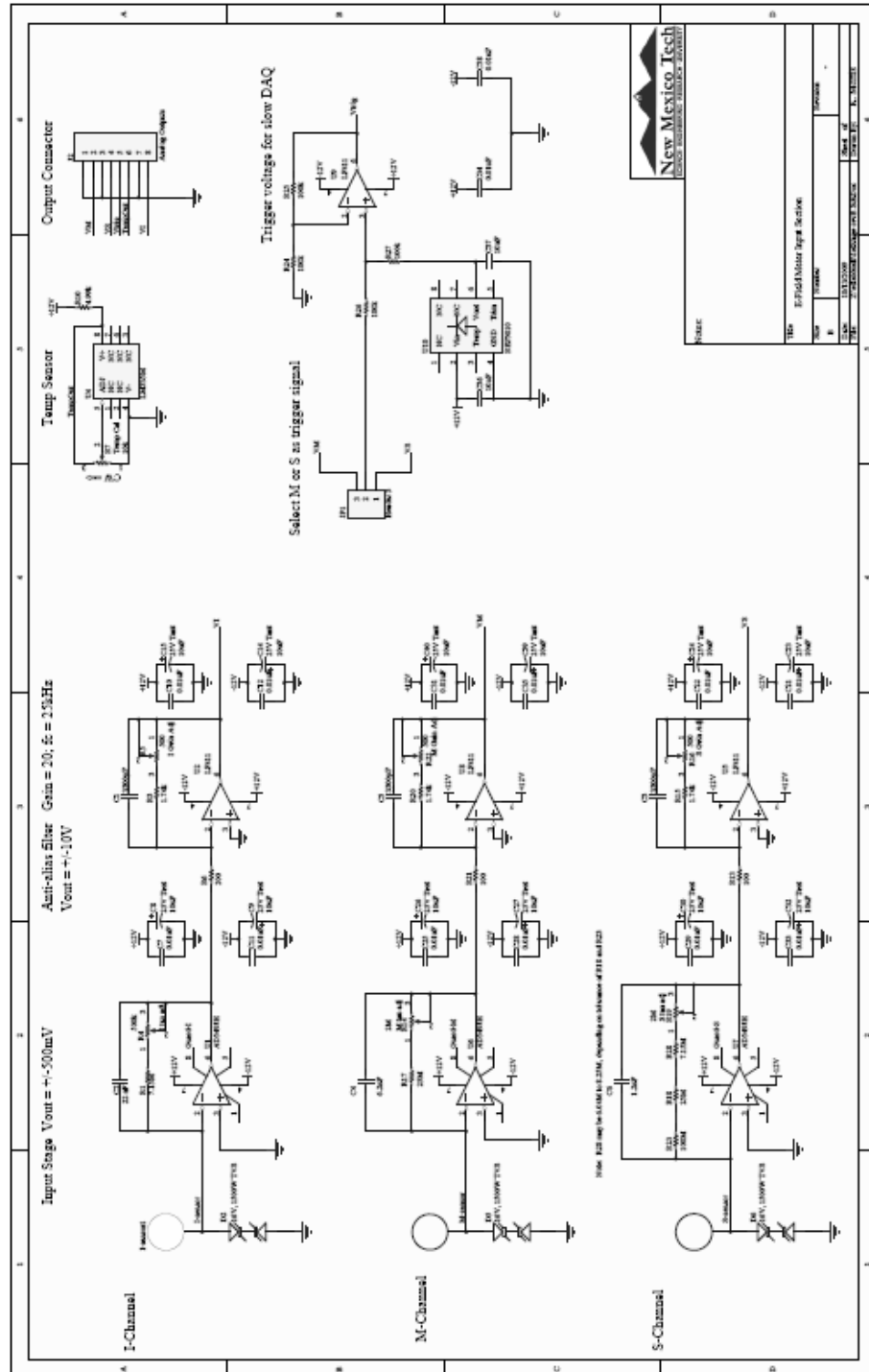
Results of second cross-calibration show (1) ratios of Puma2/Puma6 range from 1.302 to 1.355, (2) ratios of Puma4/Puma6 and Puma5/Puma6 are around 0.588-0.733, 0.702-0.734, respectively, (3) ratios of Puma7/Puma6 vary between 2.088 and 2.216, (4) ratios of Puma8/Puma6 is between 0.983 and 1.066. The most sensitive instruments are located on the roof of Workman Center (Puma2) and on a mountain ridge near the Langmuir Lab Balloon Hangar (Puma7), because of the E-field distortion around elevated objects. Puma8/Puma6 ratio is reasonable and close to what expected, because both of them share the same shape of ground. While Puma4/Puma6 and Puma5/Puma6 is lower than 1, and currently the reason still is unknown. The gain ratios that were determined experimentally during second cross-calibration will be used to scale measurements accordingly and correlate stages of a lightning strike across stations in the post data analysis.

Initial test data show that the type of lightning flash, cloud-to-ground (CG) or intra-cloud (IC), is easy to distinguish by visually inspecting the electric field waveforms acquired at multiple stations. The measurements of this new array of instruments for a negative CG flash and an IC flash are consistent with current understanding of lightning. Making simultaneous measurements at multiple

locations enables one to clearly see expected field-reversal effects in both CG leaders and IC flashes.

APPENDIX A Schematic of Analog Board -Version B

Version B design of the analog board of FC meter is composed of three-channel circuits, trigger circuit, temperature sensor circuit and output connector.



APPENDIX C Data-Acquisition-Module (DAM) Datasheet

[Adapted from a Document]

The data acquisition module of Langmuir Electric Field Array (LEFA) is integrated in an aluminum box from Hammond Manufacturing. It is a key component in array operation. This document aims to introduce the basic components of DAM and specific connections inside of DAM box. Table C.1 shows the abbreviation convention used in this section.

A: Analog	F: Fast
AD: Analog-to-Digital	M: Module/Measurement
B: Board	PL: Plate
BRG: Bridge	PN: Panel
C: Computer/Connector	S: Slow
D: Digital	T: Temperature
E: Expansion	

Table C.1 Abbreviation Convention

I DAM Box Basic Components

DAM Box consists of 3 peripheral parts and 11 internal parts:

The 3 peripheral parts include:

- 1). **H**ammond **B**ox (**HBX**), Hammond Manufacturing
- 2). **F**ront **P**anel (**FPN**), Workman Model Shop
- 3). **B**ase **P**late (**BPL**), Workman Model Shop

The 11 internal parts include:

- 1). Puma PC104-Plus **S**ingle **B**oard **C**omputer (**SBC**), Versallogic corporation
- 2). **I**/O **E**xpansion **M**odule (**IEM**), Versallogic corporation
- 3). **H**ard **D**isk **D**rive (**HDD**), Hitachi
- 4). STX104 Integrated Analog PC/104 Card with One Mega-Sample FIFO, as for **F**ast **A**/D converter (**FAD**), Apex Embedded Systems
- 5). **F**ast **I**/O **C**onnecter (**FIC**), as for FAD, Apex Embedded Systems
- 6). TS-9700 PC/104 12-bit A/D Conversion Daughter Board, as for **S**low **A**/D converter (**SAD**), Technologic Systems
- 7). WILIGEAR CPU Board WBD-111 with mini-PCI radio WMR-400 (wireless network card), as for wireless **B**ridge (**BRG**), Wiligear
- 8). **G**PS Signal Conditioning **B**oard (**GPB**), Student Built
- 9). **T**emperature **M**easurement **B**oard (**TMB**), Student Built
- 10). DC/DC **C**onvertr (**CVT**), Lambda
- 11). **F**ilter **B**oard (**FB**), Student Built

II DAM Box Layout

a). Front Panel Layout

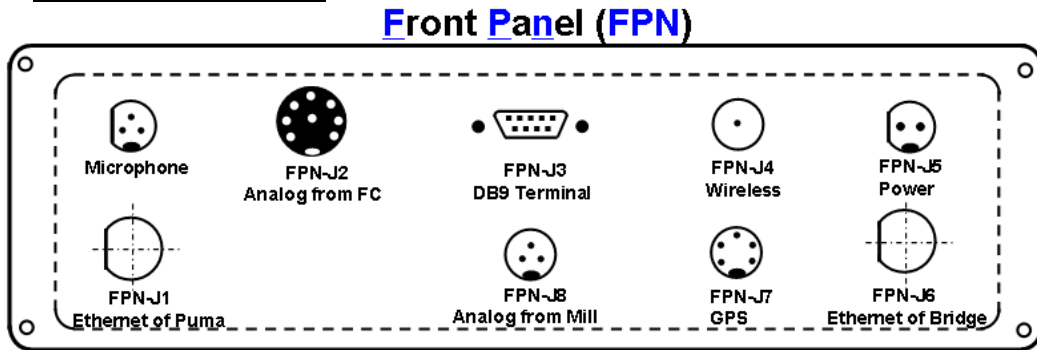


Figure C.1 Front Panel Layout

b). Base Plate Layout

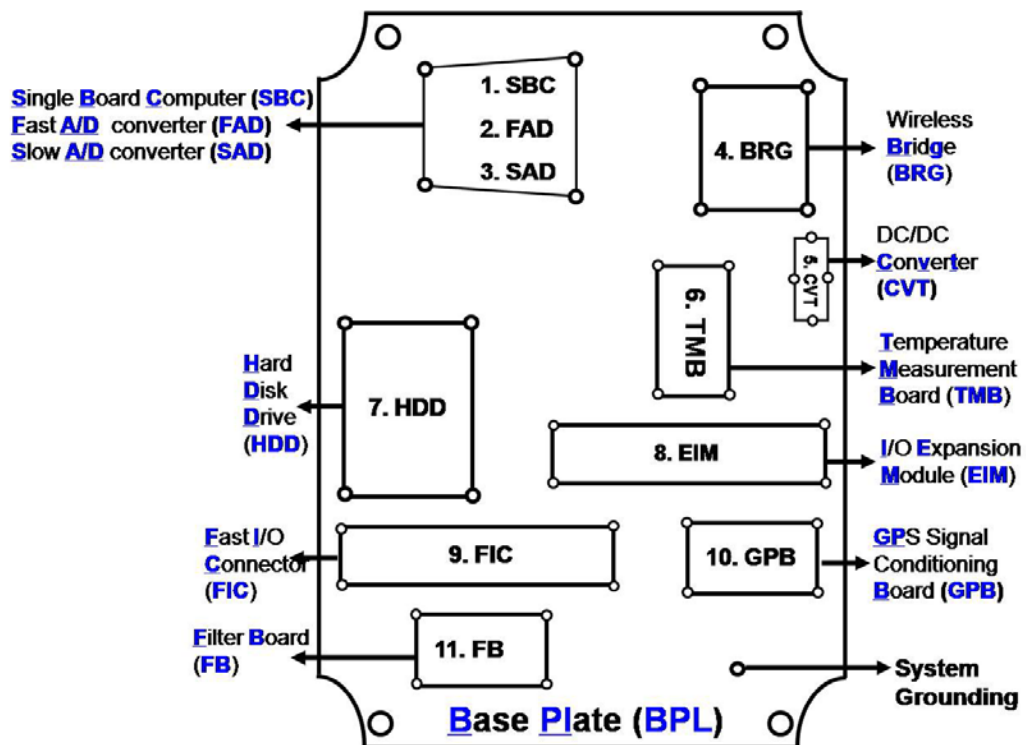


Figure C.2 Base Plate Layout

III DAM Box Connection

a). Front Panel Connection

Connector No.	Name	From	To	Comment
FPN-J1	Ethernet of Puma	FPN-J6	SBC-J4	Wired Network
FPN-J2	Analog of FC Meter	FC Meter	FB-J1&J2 SAD-J6 (Temp.) SAD-J7 (Trigger)	Field Change Analog Input
FPN-J3	DB9 Terminal	Laptop	IEM-J3	Local Debug (miniCOM)
FPN-J4	Wireless Connection	Wireless Antenna	BRD-J5	Wireless Communication
FPN-J5	Power	Battery Bank	CVT-pin2(-),3(+)	Power Supply
FPN-J6	Ethernet of Bridge	FPN-J1	BRG-ET	Wired Network
FPN-J7	GPS port pin4,5	GPS Antenna	GPB-J2 pin2(TX), pin3(PPS)	GPS Info Input
	GPS port pin1,2	CVT-pin4(COM), pin6(+5V)	GPS Antenna	Power Supply for GPS
FPN-J8	Analog of Meter	Field Mill	SAD-J4(Insensitive) SAD-J5(Sensitive)	Field Analog Input

Table C.2 Front Panel (FPN) Connection

1). FPN-J1 and FPN-J6 (RJ45 Jack)

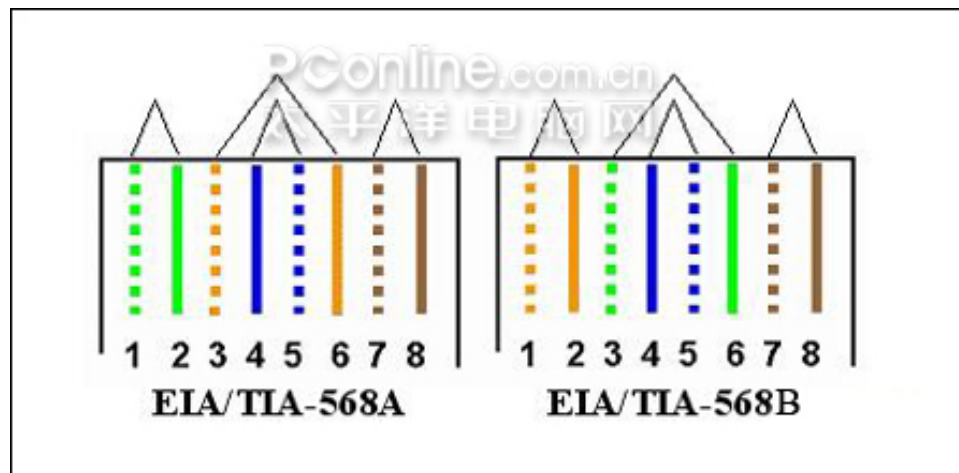


Figure C.3 Ethernet 568B Cable RJ45 Jack Configuration Standard

2). FPN-J2 (8 pin Connect Socket)

8pin Conn.	1	2	3	4	5	6	7	8
FC meter	I chan.	I return	M chan.	M return	S chan.	S return	Temp.	Trigger

Table C.3 8 pin Connector Configuration

3). FPN-J3 (Female DB9)

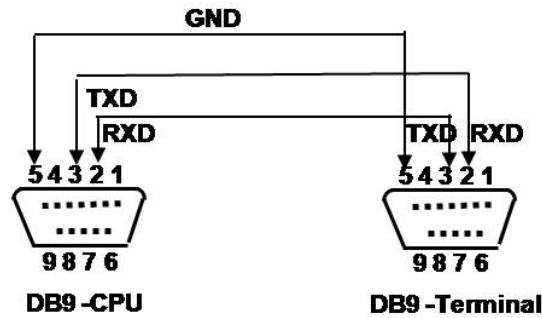


Figure C.4 DB9 Configuration

4). FPN-J4 (N-Female Bulkhead)

5). FPN-J5 (2 pin Connect Pin)

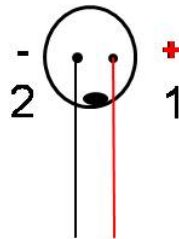


Figure C.5 2 pin Connector Configuration

6). FPN-J7 (5 pin Connect Pin)

5pin Conn.	1	2	3	4	5
GPS	+5V	GND	idle	TX	PPS

Table C.4 5 pin Connector Configuration

7) FPN-J8 (3 pin Connect Pin)

3pin Conn.	1	2	3
Field Mill	I chan.	S chan.	GND

Table C.5 3 pin Connector Configuration

b). Internal Parts Connection

1). Puma PC104-Plus Single Board Computer (SBC)

What is it?

This is a single board computer with an AMD GX 500 processor. The board is compatible with popular operating systems including Linux. A full complement of standard I/O ports is included on the board. I/O expansion for data acquisition is available through the high-speed PC/104-Plus (PCI) and PC/104 (ISA) connectors.

What is it used for?

Data acquisition and processing.

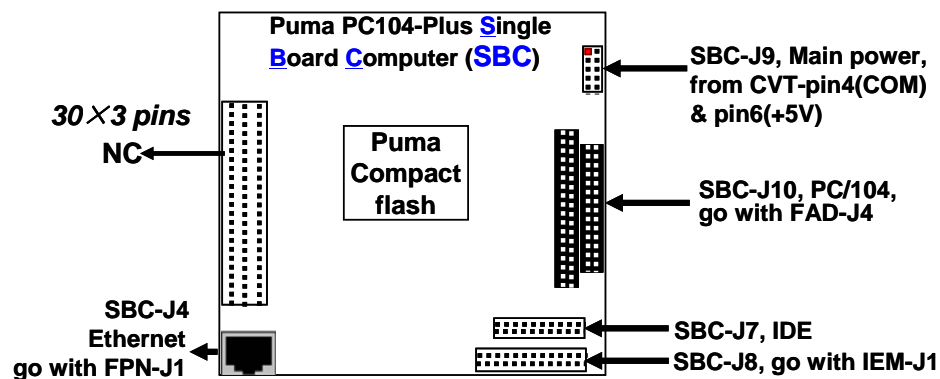


Figure C.6 Puma PC104-Plus Single Board Computer (SBC) Connectors Location

Connector No.	SBC-J4	SBC-J7	SBC-J8	SBC-J9	SBC-J10
Name	Ethernet	IDE	Standard I/O	Main Power	PC/104
Comment	FPN-J1	HDD	IEM-J1	CVT-pin4(CO M)&pin6(+5V)	FAD-J4

Table C.6 Puma PC104-Plus Single Board Computer (SBC) Connection

2). I/O Expansion Module (IEM)

What is it and what is it used for?

Provides access to DB9 serial ports of SBC (puma). It is used for terminal communication with laptop through miniCOM.

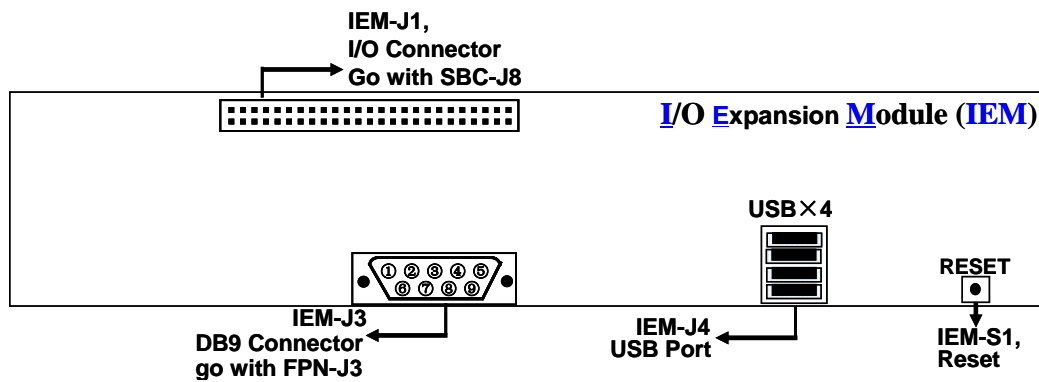


Figure C.7 I/O Expansion Module (IEM) Connectors Location

Connector No.	IEM-J1	IEM-J3	IEM-S4	IEM-S1
Name	Extended I/O Connector	DB9 Connector	USB port	Reset
Comment	Go with SBC-J8	Go with FPN-J3	connect USB keyboard for debug.	Press To reboot puma (SBC).

Table C.7 I/O Expansion Module (IEM) Connection

3). **Hard Disk Drive (HDD)**

What is it used for?

Storing data files. It is configured to DEVICE1 by setting jumpers as shown in Figure C.8. As Table C.2 shown, it will connect to SBC-J7.

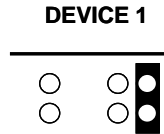


Figure C.8 5 HDD Jumpers Setting

4). **STX104 Integrated Analog PC/104 Card with One Mega-Sample FIFO, as for Fast A/D converter (FAD)**

What is it?

The STX104 is a 16-channel 16-bit A/D card, which incorporates a large one mega-sample FIFO. It has been configured to 8 differential channels rather than 16 single ended channels.

What is it used for?

The 8-channel 16-bit differential analog to digital converter (ADC) is used to acquire the change of the electric field (FC Meter) data, and to digitize GPS output. The optional 2-channel analog outputs are not used in application.

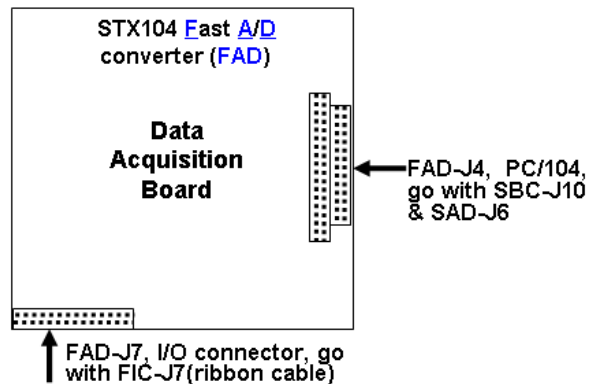


Figure C.9 STX104 Integrated Analog PC/104 Card (FAD) Connectors Location

Connector No.	FAD-J4	FAD-J7
Name	PC/104	I/O Connector
Comment	Go with SBC-J10 & SAD-J6	Go with FIC-J7

Table C.8 STX104 Integrated Analog PC/104 Card (FAD) Connection

Jumpers setting of STX104

The pins that need to be jumpered are **M0, M1, M2, A8, A9**.

The pin that doesn't need to be jumpered is **J8**.

5). VARIOFACE-Module, as for Fast I/O Conductor, (FIC)

What is it?

VARIOFACE COMPACT-LINE modules connect ribbon cable connections in accordance with IEC 603-1/DIN 41 651 to screw and spring cage connection terminal blocks for conductor cross sections of up to 1.5 mm.

What is it used for?

It works as the input connector with screw pins for FAD.

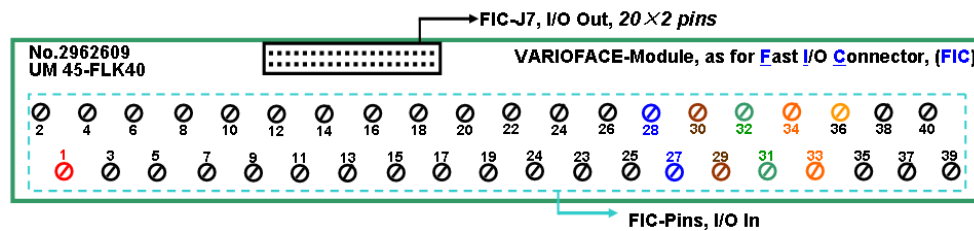


Figure C.10 Fast I/O Connectors (FIC) Location

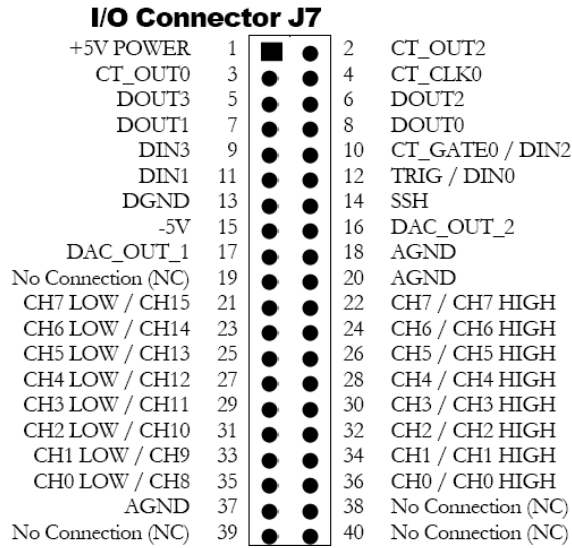


Figure C.11 Fast I/O Connectors (FIC) Specification

Connector No.	FIC-Pins	FIC-J7
Name	I/O In	I/O Out
Comment	Go with FB&GPB-J3	Go with FAD-J7(ribbon cable)

Table C.9 Fast I/O Connector (FIC) Connection

Channel Name	Channel No.	FIC-Pins No.	FB Pins No.	Wire color
GPS	0	36		yellow
		35		black
Insensitive	1	34	1	orange
		33	2	orange & white
Medium	2	32	3	green
		31	4	green & white
Sensitive	3	30	5	brown
		29	6	brown & white

Table C.10 Fast I/O Connector (FIC) Pin-Out Details

6). TS-9700 PC/104 12-bit A/D Conversion Daughter Board, as for Slow A/D converter (SAD)

What is it?

The Technologic Systems TS-9700 is a PC/104 daughter board that provides 8 channels of 12-bit Analog-to-Digital (A/D) conversion using a precision 0.2% analog reference. The Analog-to-Digital conversion takes 9 microseconds to complete allowing up to 100K samples per second.

What is it used for?

Slow data acquisition (<10 samples/s) for 1).field mill, 2).temperature of hard drive, Hammond Box, and FC meter, 3).voltage of battery, and 4). Trigger signal

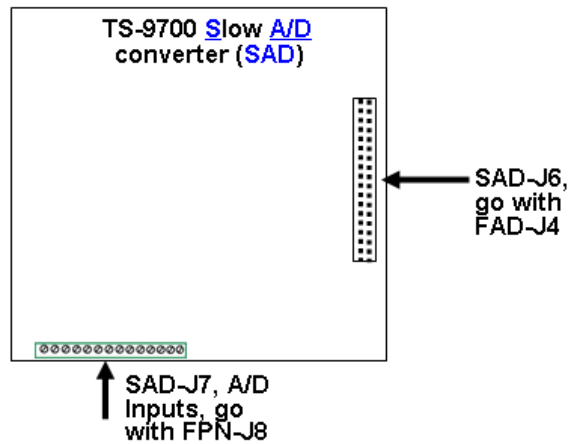


Figure C.12 TS-9700 A/D Conversion Daughter Board (SAD) Connectors Location

Connector No.	SAD-J6	SAD-J7
Name	PC/104	A/D Inputs
Comment	Go with FAD-J4	Go with FPN-J8

Table C.11 TS-9700 A/D Conversion Daughter Board (SAD) Connection

Channel Name (Inputs)	SAD-J7 Channel No.	From	Wire color
Battery Bank	1	TMB	red
Temp. of Puma box	2	TMB-J1	red
Temp. of HDD	3	TMB-J2	red
Insensitive of Field Mill	4	FPN-J8 Pin-1	red
Sensitive of Field Mill	5	FPN-J8 Pin-2	yellow
Temp. of FC meter	6	FPN-J2 Pin-7	blue
Trigger	7	FPN-J2 Pin-8	blue & white
Reserved	8		

Table C.12 SAD-J7 Pin-Out Details

Jumpers setting of TS9700:

The pins what need to be jumpered are **C1, C2, C3,C4, C5, C6, C7, C8** and **JP3**.

Jumper description: 0.1” headers [CAT SJ-1 from all electronics].

7). WILIGEAR kit, as for wireless Bridge (BRG)

What is it?

CPU board WBD-111 is a small and fast single board computer designed for point-to-point and point-to-multipoint wireless bridges, wireless mesh repeaters and 802.11 access points. It is configured with the WILIGEAR mini-PCI radio WMR-400 for the wireless communications of the LEFA.

Mini-PCI radio WMR-400 is a dual band 802.11 a/b/g, high power wireless network mini-PCI adapter based on the Atheros AR5414A(-B2B) chipset. It has 400 miliwatts of RF output power and is specifically designed for outdoor access points. The RF output connector is MMCX.

What is it used for?

Wireless Communications and Remote Power Control.

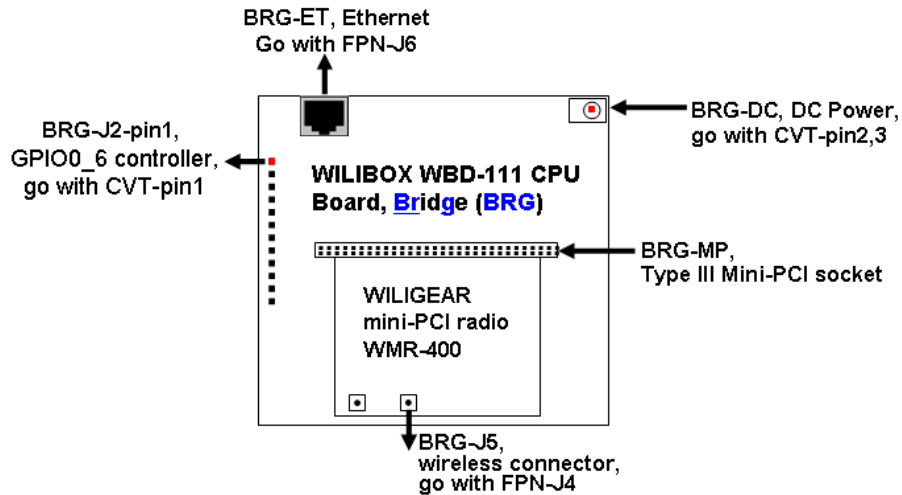


Figure C.13 WILLBOX CPU Board (Bridge) Connectors Location

Connector No.	BRG-ET	BRG-DC	BRG-J2-pin1	BRG-MP	SAD-J5
Name	Ethernet (I/O)	DC Power (In)	GPIO0_6 Controller (Output)	Type III Mini-PCI socket (I/O)	Wireless connector (I/O)
Comment	FPN-J6	CVT-pin 2,3	CVT-pin1 (enable/disable system power)	WILIGEAR mini-PCI radio	FPN-J4

Table C.13 WDB-111 CPU Board, Bridge (BRG) Connection

Configuration

It can work as the WAP through running the wili-ap (WILI Access Point) skin, also it can work as the client bridge on the station side by running the wili-cpe (WILI Customer Premises Equipment) skin with the bridge operating mode. On both WAP side and station side, the WBD-111 CPU boards are set to 'WDS' mode. WDS is the abbreviation for Wireless Distribution System. It is a system that enables the wireless interconnection of access points in IEEE 802.11 network. It allows a

wireless network to be expanded using multiple access points without the need for a wired backbone to link them, as is traditionally required. The Service Set identifier (SSID) is set to 'luckybamboo', which is a name that identifies a particular 802.11 wireless LAN. The parameter 'ACK timeout' setting depends on 15 km of the distance between WAP and client point and the antenna gain 19 dBi. Table C.14 shows the wireless settings of WILIGEAR CPU boards. As shown in Figure 2.8, the client bridge is also integrated in the DAM box only for the purpose of convenience. It is configured with IP address of Langmuir network as well as the SBC of DAM.

IEEE mode	G
SSID	luckybamboo
Channel	3
Station mode	WDS
Data rate, Mbps	54
ACK timeout	150

Table C.14 Wireless Settings of WILIGEAR CPU Board

8). **GPS Signal Conditioning Board (GPB)**

What is it & what is it used for?

This is a GPS board for integrating PPS signal and TX signal using NAND gate operation.

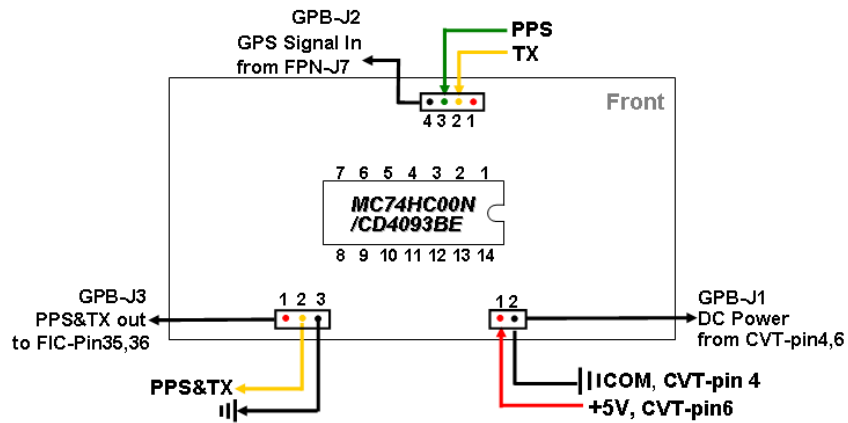


Figure C.14 GPS Signal Conditioning Board (GPB) Location

Connector No.	GPB-J1	GPB-J2	GPB-J3
Name	DC Power (in)	GPS Signal In	PPS&TX out
Comment	From CVT-pin4(COM),6(+5V)	From FPN-J7	To FIC-Pin35,36

Table C.15 GPS Signal Conditioning Board (GPB) Connection

9). **Temperature Measurement Board, (TMB)**

What is it and what is it used for?

This is a temperature measurement board for measuring temperature of hard disk drive and inside temperature of Hammond Box.

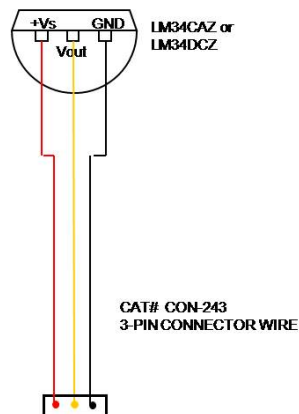


Figure C.15 Temperature Sensor Cable Layout

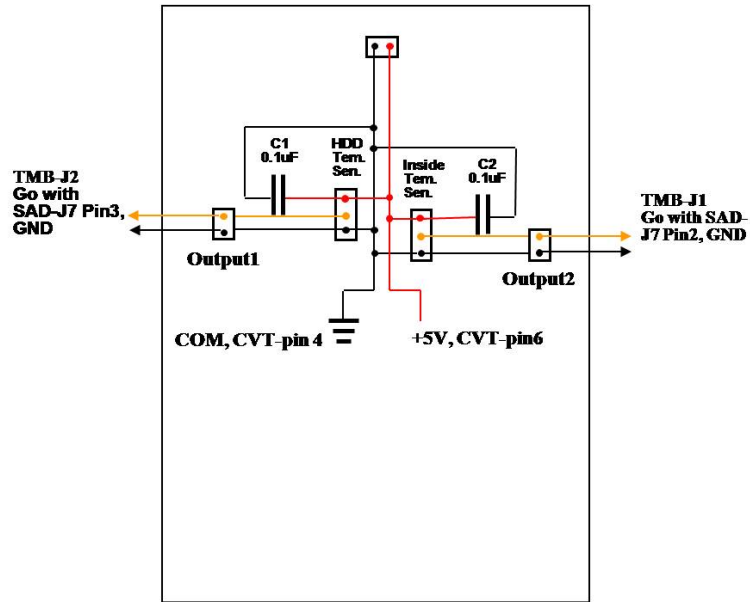


Figure C.16 Temperature Measurement Board (TMB) Location

10). DC/DC Converter (CVT)

What is it?

The DC-DC converter provides a fully isolated and regulated output at power levels up to 20 watts. It accepts a wide range DC input. The converter may be operated with or without the input and output pins grounded.

What is it used for?

It converts power from +12V to +5V and then provides power supply for puma (SBC), GPS, GPB, TMB.

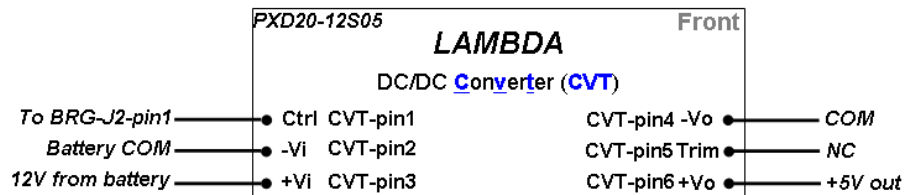


Figure C.17 DC/DC Converter (CVT) Connectors Location

Pin num	Mark	Comment
---------	------	---------

CVT-pin1	Ctrl	Controller connector, allows WILIBOX to turn on/off system power
CVT-pin2	-Vi	COM
CVT-pin3	+Vi	+12V from Battery
CVT-pin4(COM)	-Vo	COM
CVT-pin5	Trim	Not Connected
CVT-pin6(+5V)	+Vo	+5V Output

Table C.16 DC/DC Converter (CVT) Connection

11). Filter Board (FB)

What is it and what is it used for?

The Filter Board contains three low-pass filters with the cut-off frequency 106 kHz. They are used to filter the noise of high frequency, which is caused by the transmission cable, from three channels of FC meter.

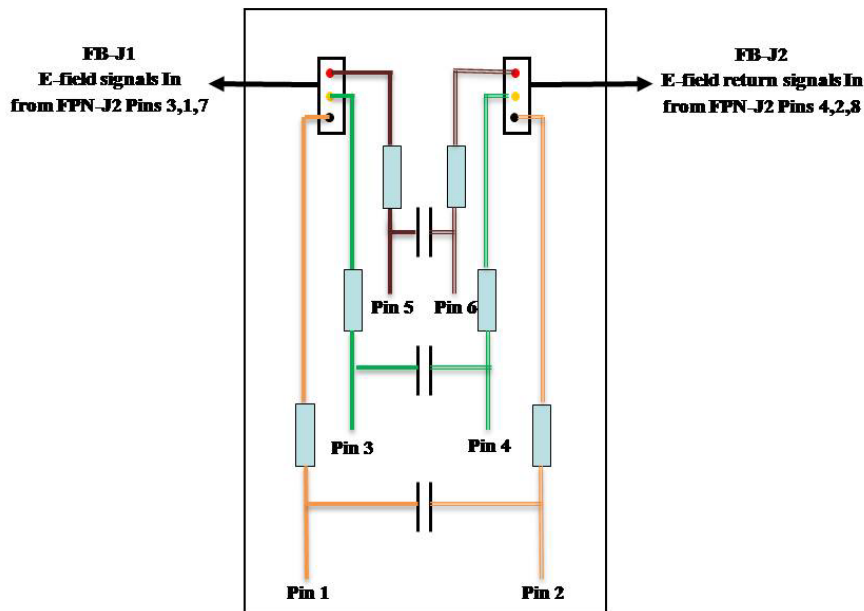


Figure C.18 Filter Board (FB) Location

APPENDIX D Test Instruction and Form

Purpose:

This instruction is to show how to test every function, cable connectivity in Data Acquisition Module (DAM) and the wireless communication function in Workman Room 324.

1. Power

To test the function and connection of the DC/DC converter.

- 1> Disconnect all outputs of CVT(DC/DC converter),
- 2> Plug power cable from 12V battery to FPN-J5,
- 3> Measure each output and record it in the test form

2. SBC—Puma-x

To test the function of SBC-Puma-x and its BISO setting.

Note: IP of Puma-x is 10.0.100.18x.

- 1> power on the SBC
- 2> check if it starts well from terminal program minicom through serial port, including if the BISO configuration screen show off in the start stage.

3. Bridge, Networking

To test if networking between WAP and Client Bridge works well.

Note: IP of bridge-x is 10.0.100.19x.

- 1> In Puma-x, ping IP of client bridge: 10.0.100.19x,

- 2> Ping IP of server bridge (also called “WAP”): 10.0.100.190,
- 3> Ping IP of server-Panda: 10.0.100.180.

4. Power control

To test if the 5 V power of DAM can be turned on or off through the output of GPIO-6 of client bridge.

- 1> Connect the pin of GPIO-6 of Bridge to the pin of crl of CVT,
- 2> In server-Wave, login to the client bridge by running the following command:
ssh admin@10.0.100.19x, and pwd is langmuir
- 3> Go to shell by inputting ‘shell’ in the command line.
- 4> Control the output of GPIO-6 by running the following commands:

```
$ cd /sbin
$ gpio -r 6          readout the default output of GPIO-6, it should be 1,
$ gpio -w 6 0       power off the CVT
$ gpio -w 6 1       power on the CVT
```

5. GPS and FC meter data

To check the function of GPS circuit board and connection between FC meter and SBC of puma-x. Wave a piece of Teflon in the front of sensor plates of FC meter and take simulative lightning data from Puma-x through FAD card by running the C program – stx104_aifile

- 1> Power on the GPS circuit board,
- 2> Connect the GPS to FPN-J7,
- 3> Connect the FC meter to FPN-J8, and power on FC meter,
- 4> Take data by running the following commands:
 - a> cd /DATA/
 - b> ./stx_ai_file -l:1200000 -o:GPS&FCtest -v

6. Temperature in DAM Box and FC meter

There are two temperature sensors installed in Hammond Box, one is to test HDD

temperature, another is to test inside-box temperature. Also there is an embedded temperature sensor in the FC meter. The SAD is used to take these temperature data and trigger data.

1> power on the temperature board and FC meter,

2> take data by running the following commands:

a> `./ts9700_aifile -i jianhua.cfg`

b> `tail -f puma4_20090320.log_ch2` – read out file

7. Field Mill data

Test Form

	Item	Time and Tester	Result (P/F)	Note
1	Power			
2	SBC—puma-x			
3	Bridge, Networking			
4	Power Control			
5	GPS and FC meter			
6	Temperatures in DAM Box and FC meter			
7	Field Mill			

REFERENCE

Bruce, C. E. R., and R. H. Golde, The Lightning Discharge, The Journal of the Institution of Electrical Engineers, Vol. 88, Part II, pp. 487-505,(1941).

Chalmers, J. A., Atmospheric Electricity, International Series of Monographs on Natural Philosophy, vol.11, 2nd ed, 515 p. Elsevier, New York, (1967).

Cummins, K. L., M. J. Murphy, E. A. Bardo, W. L. Hiscox, R. B. Pyle, and A. E. Pifer (1998), A combined TOA/MDF technology upgrade of the U.S. National Lightning Detection Network, *J. Geophys. Res.*, *103*, 9035-9044.

David J. Griffiths, 'Introduction to Electrodynamics', 3rd edition.

Hager W. W., Sonnenfeld R. G., and B. C. Aslan (2009), Three Dimensional Charge Structure of a Mountain Thunderstorm, *J. Geophys. Res.*, DOI:10.1029/2009JD13241.

Hager W. W., and Sonnenfeld R. G. (2007), CMG Collaborative Research in Measurement and Analysis of Thunderstorm Electrification and Lightning, Proposal to the National Science Foundation.

Hager W. W., Sonnenfeld R. G., B. C. Aslan, G. Lu, W. P. Winn, and W. L. Boeck (2007), Analysis of charge transport during lightning using a balloon borne electric field sensors and Lightning Mapping Array, *J. Geophys. Res.*, *112*, D18204, doi:10.1029/2006JD008187.

<http://www.macslab.com/optosolar.html>, 'Optimum Orientation of Solar Panels', Oct., 2008.

<http://www.duxlite.com/enlarge/pump/solar%20sizing.pdf>, 'Solar Sizing Guide', Oct., 2008.

<http://www.weather-plus.net/LightningDetector.html>, Nov., 2009.

<http://www.movable-type.co.uk/scripts/latlong.html>, Nov., 2009.

<http://en.wikipedia.org/wiki/Lightning#Types>, Nov., 2009.

http://www.pc104.org/pc104_specs.php, Nov., 2009.

Idone V. P., D. A. Davis, P. K. Moore, Y. Wang, R. W. Henderson, M. Ries, and P. F. Jamason (1998), Performance evaluation of the U. S. National Lightning Detection Network in eastern New York: 2. Location accuracy, *J. Geophys. Res.*, *103*, 9057-9069.

Krehbiel P. R., M. Brook, and R. A. McCrory (1979), An analysis of the charge structure of lightning discharges to ground, *J. Geophys. Res.*, *84*, 2432-2456.

Krehbiel, P. R. (1981), An analysis of the electric field change produced by lightning, Ph. D. dissertation, Univ. of Manchester Inst. of Science and Technology.

Lay E. H., R. H. Holzworth, C. J. Roger, J. N. Thomas, O. Pinto Jr., and R. L. Dowden (2004), WWLL global lightning detection system: Regional validation study in Brazil, *Geophys. Res. Lett.*, *31*, L03102, doi:10.1029/2003GL018882.

Lu G., W. P. Winn, and R. G. Sonnenfeld (2009), Analysis of Charge transfer in intracloud lightning using a time-dependent multi-dipole model, *J. Geophys. Res.*, DOI:10.1029/2009JDxxxxxx. In preparation.

MacGorman D. R., and W. D. Rust (1998), *The electrical nature of storms*, New York, Oxford Univ. Press.

Rakov V. A., and M. A. Uman (2003), *Lightning: Physics and effects*, New York, Cambridge Univ. Press.

Reynolds S. E., and H. W. Neill(1955), The distribution and discharge of

thunderstorm charge centers, *J. Meteorol.*, 12, 1-12.

Rison, W., R. J. Thomas, P. R. Krehbiel, T. Hamlin, and J. Harlin (1999), A GPS-based three-dimensional lightning mapping system: Initial observations in central New Mexico, *Geophys. Res. Lett.*, 26, 3573-3576.

Shao, X.-M., M. Stanley, A. Regan, J. Harlin, M. Pongratz, and M. Stock (2006), Total lightning observations with the new and improved Los Alamos Sferic Array (LASA), *J. Atmos. Oceanic Tech.*, 23, 1273-1288.

Sonnenfeld, R. G., J. D. Battles, G. Lu, and W. P. Winn (2006), Comparing E field changes aloft to lightning mapping data, *J. Geophys. Res.*, 111, D20209, doi:10.1029/2006JD007242.

Uman M. A. (1987), *The lightning discharge*, Orlando, Academic Press.